Journal of Operation and Automation in Power Engineering

vol. XX, no. XX, Dec. 2022, Pages: XXXX (Proofed)

http://joape.uma.ac.ir

Super-Twisting Control for a Doubly Fed Induction Generator (DFIG)-Based Wind Turbine Using a Nonlinear Observer

H. Bahlouli[1,*], *A. Mansouri*[2], *M. Bouhamida*[1]

[1] *AVCIS Laboratory, Automation Department, University of Science and Technology Mohamed Boudiaf, El Mnaouar, BP 1505, Bir El Djir 31000, Oran, Algeria*

[2] *LAAS laboratory, Electrical Engineering Department, Polytechnic School Maurice Audin of Oran, El Mnaouer, BP 1523 Oran, Algeria*

Abstract— *The high cost and complexity of using sensors for controlling processes have led to the development of observer techniques that aim to estimate system states without the need for sensors. These techniques reduce system complexity and can potentially reduce product and maintenance costs. In this paper, we present an interconnected high gain observer (IHGO) that estimates the electromagnetic torque, speed, and position of a doubly fed induction generator-based wind turbine (DFIG-WT) using only voltage, current, and wind speed measurements. The IHGO is designed to be robust to parameter uncertainties and its stability is assessed using Lyapunov theory. To guarantee finite time convergence, a Super Twisting-based High Order Sliding Mode (ST-HOSM) controller is used for direct torque control. The ST-HOSM is a simple algorithm that maintains the sliding mode characteristics, provides robustness against disturbance, and reduces the chattering phenomenon. The controller and observer are designed in the $\alpha\beta$ frame to avoid the use of a phase-locked loop (PLL). Simulation results confirmed the effectiveness of the proposed control strategy under parameter uncertainties, power and speed variations, grid voltage dip and current sensor noise.*

Keywords—Direct torque control, High gain observer, Nonlinear observer, Sensorless control, Wind energy conversion system.

NOMENCLATURE

Ω_a, Ω_m	Turbine and rotor speed (rpm).
ω_s, ω_m	Stator and generator angular speed (rad/s).
g	Slip (%).
L_s, L_r, L_m	Stator, rotor and mutual inductances (H).
R_s, R_r	Stator and rotor resistances (Ω).
σ	Leakage coefficient $\sigma = 1 - {L_m}^2/L_s L_r$
$v_{s\alpha}, v_{s\beta}, v_{r\alpha}, v_{r\beta}$	Stator and rotor $\alpha\beta$ frame voltages (V).
$i_{s\alpha}, i_{s\beta}, i_{r\alpha}, i_{r\beta}$	Stator and rotor $\alpha\beta$ frame currents (A).
P_m, P_s, Q_s	Mechanical (W), stator active (W) and reactive power (VARW).
C_p	Power coefficient
G	Gearbox ratio
ρ	Air density (kg/m^3)
R	Radius of the blade (m)
T_a, T_{em}, T_m	Aerodynamic, electromagnetic and mechanical torque (N.m).
f_v	Friction coefficient (Nm.s/rad).
J	Inertia of the rotating part (kg.m^2).
V_w	Wind speed (m/s).
λ	Speed ratio.
p	Pole pairs.
${T_{em}}^*, {Q_s}^*$	Electromagnetic torque and reactive power references.
β	Angle of the blade (°).
V_s	Grid voltage (V).
f	Grid frequency (Hz).

Received: 13 Oct. 2022
Revised: 27 Feb. 2023
Accepted: 08 Jun. 2023
*Corresponding author:
E-mail: hakima.bahlouli@univ-usto.dz (H. Bahlouli)
DOI: 10.22098/joape.2023.11663.1873
Research Paper

1. INTRODUCTION

According to the World Wind Energy Association, wind power plants globally have installed a capacity of 744 GW, of which 707 GW was supplied by onshore plants in 2020. This energy can meet 7% of the global demand for electricity [1]. Wind power is the fastest-growing source of renewable energy, and manufacturers are aiming to increase wind energy conversion system (WECS) production capacity. One wind turbine can produce 7.2 MW [2], while an offshore installation can generate 15 MW [3]. The generator is a key part of the WECS, and due to its several advantages, the doubly fed induction generator (DFIG) is a commonly used machine for generating wind energy. Its converter receives approximately 25 to 30 percent of the generator's entire rated power, which helps to reduce cost and power loss. However, the DFIG-based wind turbine (DFIG-WT) is a dynamic and complex system, and control research issues is a relevant investment for this wind energy system [4].

Vector control (VC) is a common control strategy used for induction machines [5]. However, it is strongly sensitive to parameter variations and uncertainties. Direct torque control (DTC) and direct power control (DPC) are popular alternative control schemes for induction machines [6, 7]. Robustness and a simple control scheme are attractive characteristics of these control methods. Regardless of their performance, the DTC/DPC techniques suffer from torque and power ripples due to converter switching frequency variations [8, 9]. Therefore, integrating nonlinear control algorithms result in a more robust control scheme [10].

High order sliding mode (HOSM) control is a popular nonlinear control method that has been extensively studied in recent years.

HOSM controllers have been designed and implemented in various control applications due to their robustness, fast convergence, and reduced chattering compared to classical sliding mode (SM) controllers [11]. One of the most commonly used HOSM controllers is the second-order sliding mode (SOSM) controller. It has been applied to control different systems, such as electrical machines [12], power converters [13], and robotics [14]. However, SOSM control requires the computation of higher-order derivatives of the sliding surface, which may lead to numerical problems and difficulties in practical implementation.

To overcome these issues, the super twisting algorithm (STA) was proposed as an alternative HOSM controller that eliminates the need for computing higher-order derivatives of the sliding surface [15]. The STA has been applied to control different systems, including wind turbines [16], electric vehicles [17], and power converters [18]. Several studies have compared the performance of SM controllers, including SOSM and STA. In [19], an HOSM controller based on the SOSM and STA was designed for the control of a DC-DC converter. The simulation results showed that the STA-based controller had better performance in terms of convergence speed and chattering reduction compared to the SOSM-based controller. Another study compared the performance of SM and STA controllers for systems with stable actuators. The aim of the comparison is to analyze the chattering parameters, which refer to the amplitude and frequency of fast oscillations produced by the controllers, as well as the average power needed to maintain the system in real sliding modes. SM controller produces greater amplitude of oscillations and requires more average power compared to the STA [20]. The Super Twisting controller is more robust against parameter variations and reduces the chattering phenomenon, leading to improved performance in terms of tracking error, time response, and robustness [21, 22].

It is necessary to have a full understanding of the process under study before creating control schemes. In fact, not all of the variables used to define the system states are subject to direct measurement. To estimate the unmeasured variables from the measured ones, numerous observation approaches have been proposed. In an industrial application, an observer can afford the option to optimize the number and cost of sensors. In recent decades, there has been widespread interest in synthesizing and investigating observation methods, especially in drive machines [23]. Estimation of fluxes and torques are common techniques assessed by researchers, in addition to position and speed estimation [24, 25]. Model reference adaptive systems (MRASs) [26, 27], linear observers [28–30], and nonlinear observers [31–33] are examples of these methods. Despite the effectiveness of MRAS and its huge application in machine drives, this observer suffers from parameter variation sensitivity and low-speed inaccuracy. The linear observer has almost the same disadvantages. On the other hand, the nonlinear observer has received much attention in recent years as a result of advancements in power electronic devices. We can cite classical and extended Kalman filters [34, 35], extended Luenberger observers [36], H∞ observers [37], sliding mode observers [38], hybrid observers [39], and the interconnected high gain observer (IHGO) [40, 41]. The IHGO presents a highly promising alternative to conventional linear observers due to its remarkable robustness against disturbances and parameter uncertainties, making it an exceptionally dependable and reliable solution for control systems in various industrial applications [42]. The IHGO can also improve the overall performance of the control system by accurately estimating the system states. This is especially important in power system applications, where accurate control is essential for efficient power generation [43]. Additionally, IHGO is less sensitive to the system model than other observers, such as the Luenberger observer and the Kalman, it is more resilient to model uncertainty [44]. In terms of computational complexity, this observer is relatively complex, but this can be mitigated by using a decentralized design. In [40], IHGO was compared to an adaptive observer, and the results showed that it exhibits adaptive performance in terms of robustness, system stability and response time. In another study [45], the same observer was applied to estimate the speed of the generator. Generally, the IHGO used to estimate the position speed, load torque, stator resistance or flux [46–50].

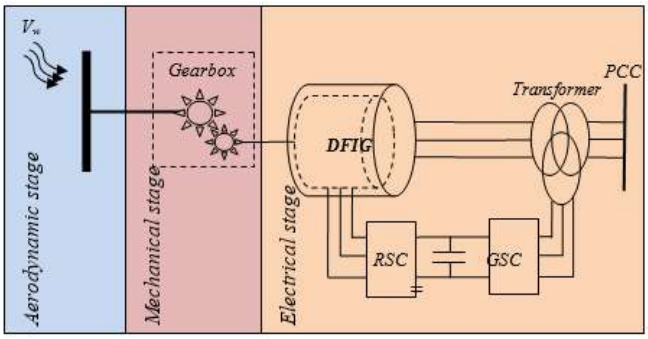

Fig. 1. WECS stages

The present paper proposes a sensorless ST-HOSM for direct electromagnetic torque and reactive power control schemes implemented in a stationary reference frame for grid-connected DFIG-WT. The main contribution of this work was to design an IHGO capable of estimating the rotor speed and electromagnetic torque utilizing voltage, current and wind speed measurements. This strategy leads to a reduction in the cost and complexity of hardware installation by eliminating speed and torque sensors. The stability of the observer was assessed by using Lyapunov theory to demonstrate the conditions in which the exponential convergence is verified. The proposed control scheme was investigated under parameter uncertainties and grid disturbances to test its performance and effectiveness. Furthermore, the stability of the observer has been highlighted in parameter uncertainties, followed by the stability of the proposed control strategy for system internal and external faults.

The remainder of this paper is organized as follows: Section 2 presents the turbine and generator dynamic models in the stationary reference frame. Section 3 is dedicated to the synthesis of control laws based on the super twisting algorithm. The design of the observers is presented in section 4. In Section 5, the performance of the proposed scheme is assessed through several computer simulations. The final section serves as a conclusion.

2. WIND ENERGY CONVERSION SYSTEM MODELING

The overall parts of WECS are basically three: aerodynamic, mechanical and electrical parts (Fig. 1).

2.1. Aerodynamic and mechanical model

In a wind turbine system, kinetic energy from the wind is converted into mechanical energy by the turbine blades. The wind is responsible for blade rotation, and this rotation will in turn spin a shaft connected to a generator [21, 51]. The system mechanical equation that describes the dynamics applied to the shaft of the generator is as follows (Fig. 2):

$$J\dot{\Omega}_m = T_{em} - T_m - f_v\,\Omega_m \tag{1}$$

The power transmitted from the wind turbine blades to the mechanical shaft is known as the generator power, and it is proportional to the aerodynamic power generated by the wind. [21, 51]:

$$P_m = 0.5\,\rho\,\pi R^2 C_p\,(\lambda,\beta)\,V_w^3/G \tag{2}$$

The power coefficient C_p is a nonlinear function that depends on the pitch angle β and tip speed ratio λ where: $\lambda = \Omega_a R/V_w$

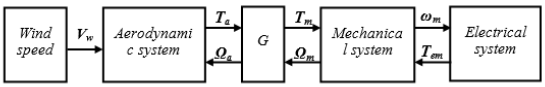

Fig. 2. Block scheme of the variable speed wind turbine model

The generator torque applied on the shaft can be expressed as follows:

$$T_m = 0.5\,\rho\,\pi R^3 C_p\,(\lambda,\beta)\,V_w^2/(G\lambda) \tag{3}$$

2.2. DFIG model

The rotor side dynamic model of the grid-connected DFIG based on the stationary reference frame is represented by[52]:

$$\begin{cases} \dot{l_{r\alpha}} &= (-R_r L_s i_{r\alpha} - \omega_m L_s L_r i_{r\beta} + L_m R_s i_{s\alpha} \\ & -\omega_m L_s L_m i_{s\beta} + L_s v_{r\alpha} - L_m v_{s\alpha})/L_r L_s \sigma \\ \dot{l_{r\beta}} &= (\omega_m L_s L_r i_{r\alpha} - R_r L_s i_{r\beta} + \omega_m L_s L_m i_{s\alpha} \\ & +L_m R_s i_{s\beta} + L_s v_{r\beta} - L_m v_{s\beta})/L_r L_s \sigma \\ \dot{l_{s\alpha}} &= (R_r L_m i_{r\alpha} + \omega_m L_m L_r i_{r\beta} - L_r R_s i_{s\alpha} \\ & +\omega_m {L_m}^2 i_{s\beta} - L_m v_{r\alpha} + L_r v_{s\alpha})/L_r L_s \sigma \\ \dot{l_{s\beta}} &= (-\omega_m L_m L_r i_{r\alpha} + R_r L_m i_{r\beta} - \omega_m {L_m}^2 i_{s\alpha} \\ & -L_r R_s i_{s\beta} - L_m v_{r\beta} + L_r v_{s\beta})/L_r L_s \sigma \end{cases} \tag{4}$$

where $v_{s\alpha\beta}, v_{r\alpha\beta}, i_{s\alpha\beta}$ and $i_{r\alpha\beta}$ are the stator and rotor voltage and current, respectively, in the stationary frame. R_s and R_r are the stator and rotor resistances, respectively. L_s, L_r and L_m are the stator, rotor and mutual inductances, respectively. ω_s and ω_m are the stator and generator angular speeds $\omega_m = p\Omega_m$.

The stator active power, reactive power and electromagnetic torque in the stationary reference frame are stated by [53]:

$$\begin{cases} P_s = 1.5\,(v_{s\alpha} i_{s\alpha} + v_{s\beta} i_{s\beta}) \\ Q_s = 1.5\,(v_{s\beta} i_{s\alpha} - v_{s\alpha} i_{s\beta}) \\ T_{em} = 1.5 L_m (i_{s\beta} i_{r\alpha} - i_{s\alpha} i_{r\beta}) \end{cases} \tag{5}$$

3. Interconnected High Gain Observer

To design an Interconnected High Gain Observer, the plant dynamics must be modeled and linearized around the operating point to form the state-space equations.

3.1. Observer design

The DFIG-WT model can be divided into two interrelated subsystems as shown below:

$$\begin{cases} \dot{l_{r\alpha}} &= (-R_r L_s i_{r\alpha} - p\Omega_m L_s L_r i_{r\beta} + L_m R_s i_{s\alpha} - p\Omega_m L_s \\ & L_m i_{s\beta} + L_s v_{r\alpha} - L_m v_{s\alpha})/L_r L_s \sigma \\ \dot{\Omega}_m &= -f_v \Omega_m/J + \ T_{em}/J - 0.5\rho\pi R^3 C_p\,(\lambda,\beta)\,V_w^2/(JG\lambda) \end{cases} \tag{6}$$

$$\begin{cases} \dot{l_{r\beta}} &= (\omega_m L_s L_r i_{r\alpha} - R_r L_s i_{r\beta} + \omega_m L_s L_m i_{s\alpha} + L_m R_s i_{s\beta} \\ & +L_s v_{r\beta} - L_m v_{s\beta})/L_r L_s \sigma \\ \dot{T}_{em} &= \frac{1.5pL_m}{L_r L_s \sigma} \begin{pmatrix} -\frac{(R_r L_s + R_s L_r)}{1.5pL_m} T_{em} - ({L_m}^2 + L_s L_r) \\ p\Omega_m\,(i_{r\beta} i_{s\beta} + i_{r\alpha} i_{s\alpha}) - L_s L_m p\Omega_m \\ ({i_{s\beta}}^2 + {i_{s\alpha}}^2) - L_m L_r p\Omega_m ({i_{r\alpha}}^2 + {i_{r\beta}}^2) + \\ L_m\,(v_{s\beta} i_{s\alpha} + v_{r\alpha} i_{r\beta} - v_{r\beta} i_{r\alpha} - v_{s\alpha} i_{s\beta}) + \\ L_s\,(v_{r\alpha} i_{s\beta} - v_{r\beta} i_{s\alpha}) + L_r\,(v_{s\beta} i_{r\alpha} - v_{s\alpha} i_{r\beta}) \end{pmatrix} \end{cases} \tag{7}$$

with: $\dot{T}_{em} = 1.5\,p\,L_m\ \left(\dot{l_{s\beta}} i_{r\alpha} + i_{s\beta} \dot{l_{r\alpha}} - \dot{l_{s\alpha}} i_{r\beta} - i_{s\alpha} \dot{l_{r\beta}}\right)$

The two subsystems (6) and (7) can be represented in compact form as follows:

$$\begin{cases} \dot{X}_1 = A_1 X_1 + g_1(u, y, X_2, X_1, V) \\ y_1 = C X_1 \end{cases} \tag{8}$$

$$\begin{cases} \dot{X}_2 = A_2 X_2 + g_2(u, y, X_1, X_2, i_{s\alpha}, i_{s\beta}) \\ y_2 = C X_2 \end{cases} \tag{9}$$

where $X_1 = \begin{bmatrix} x_1 \\ x_3 \end{bmatrix} = \begin{bmatrix} i_{r\alpha} \\ \Omega_m \end{bmatrix}$; $X_2 = \begin{bmatrix} x_2 \\ x_4 \end{bmatrix} = \begin{bmatrix} i_{r\beta} \\ T_{em} \end{bmatrix}$ are the states, $u = [u_1, u_2, u_3, u_4]^T = [v_{r\alpha}, v_{r\beta}, v_{s\alpha}, v_{s\beta}]^T$ the inputs, and $y = \begin{bmatrix} y_1 \\ y_2 \end{bmatrix} = \begin{bmatrix} i_{r\alpha} \\ i_{r\beta} \end{bmatrix}$ the outputs of the DFIG-WT.

$$A_1 = \begin{pmatrix} -R_r/(L_r\sigma) & 0 \\ 0 & -f_v/J \end{pmatrix}\ ;\ C = \begin{pmatrix} 1 & 0 \end{pmatrix}$$

$$A_2 = \begin{pmatrix} -R_r/(L_r\sigma) & 0 \\ 0 & -(R_r L_s + R_s L_r)/(L_r L_s \sigma) \end{pmatrix}$$

$$g_1 = \begin{bmatrix} (-px_3 L_s L_r x_2 + L_m R_s i_{s\alpha} - px_3 L_s L_m i_{s\beta} + L_s u_1 \\ -L_m u_3)/(L_r L_s \sigma) x_4/J - 0.5\rho\pi R^2 C_p V^3/(JGx_3) \end{bmatrix}$$

$$g_2 = \begin{bmatrix} (px_3 L_s L_r x_1 + px_3 L_s L_m i_{s\alpha} + L_m R_s i_{s\beta} + L_s u_2 \\ -L_m u_4)/(L_r L_s \sigma) \\ \frac{1.5pL_m}{L_r L_s \sigma} \begin{pmatrix} -({L_m}^2 + L_s L_r)\, px_3\,(x_2 i_{s\beta} + x_1 i_{s\alpha}) \\ -L_s L_m p x_3\,({i_{s\beta}}^2 + {i_{s\alpha}}^2) - L_m L_r p x_3 \\ ({x_1}^2 + {x_2}^2) + L_m (u_4 i_{s\alpha} + u_1 x_2 \\ -u_2 x_1 - u_3 i_{s\beta}) + L_s\,(u_1 i_{s\beta} - u_2 i_{s\alpha}) \\ +L_r\,(u_4 x_1 - u_3 x_2) \end{pmatrix} \end{bmatrix}$$

On the basis of the measurement of rotor and stator current, rotor and stator voltage, and wind speed (see Fig. 4), we sought to design two interconnected observers for subsystems (8) and (9) to estimate the rotor speed and the electromagnetic torque. Some necessary properties have been supposed before synthesizing observers.

Remark 1: We assume that $C_p(\lambda, \beta)$ is known and provided by the manufacturer (Fig. 3) and *that* ω_s is also known and supposed to be constant.

Assumption 1:

- (u, y, X_2, V) and $(u, y, X_1, i_{s\alpha}, i_{s\beta})$ are known signals for subsystems (8) and (9), respectively.
- (u, y, X_2, V) and $(u, y, X_1, i_{s\alpha}, i_{s\beta})$ are bounded and regularly persistent inputs for subsystems (8) and (9), respectively.
- g_1 is globally Lipschitz with respect to X_2 uniformly with respect to (u, y, V)
- g_2 is globally Lipschitz with respect to X_1 uniformly with respect to $(u, y, i_{s\alpha}, i_{s\beta})$

Then, assuming that the above assumption is verified, the IHGOs for subsystems (8) and (9) are given by:

$$\begin{cases} \dot{\hat{X}}_1 = A_1 \hat{X}_1 + \hat{g}_1\left(u, y, \hat{X}_2, \hat{X}_1, V\right) + S_{\alpha 1}^{-1} C^T C (X_1 - \hat{X}_1) \\ \hat{y}_1 = C \hat{X}_1 \end{cases} \tag{10}$$

$$\begin{cases} \dot{\hat{X}}_2 = A_2 \hat{X}_2 + \hat{g}_2\left(u, y, \hat{X}_1, \hat{X}_2, i_{s\alpha}, i_{s\beta}\right) + S_{\alpha 2}^{-1} C^T C (X_2 - \hat{X}_2) \\ \hat{y}_2 = C \hat{X}_2 \end{cases} \tag{11}$$

where $\hat{X}_1 = \begin{bmatrix} \hat{x}_1 \\ \hat{x}_3 \end{bmatrix}$ is the estimated vector of X_1 and $\hat{X}_2 = \begin{bmatrix} \hat{x}_2 \\ \hat{x}_4 \end{bmatrix}$ is the estimated vector of X_2 $\hat{g}_1$ is the estimated function of g_1, and $\hat{g}_2$ is the estimated function of g_2.

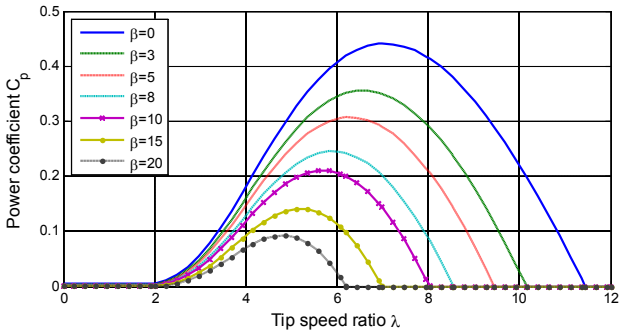

Fig. 3. Power coefficient curve

The solution of the following Lyapunov algebraic equation is the symmetric positive definite matrix S_{α_i}, and α_i is a positive constant:

$$\dot{S_{\alpha_i}} = \alpha_i S_{\alpha_i} + A_i^T S_{\alpha_i} + S_{\alpha_i} A_i - C^T C; \quad i \in \{1,2\}$$

Remark 2: It is worth noting that S_{α_1} and S_{α_2} are bounded for sufficiently large α_1 and α_2 due to the persistence of inputs considered in Assumption 1.

3.2. Stability study of the IHGO under parameter uncertainties

A stability analysis based on Lyapunov theory is presented to demonstrate the state convergence of the proposed observer.

Consider the errors:

$$\begin{cases} e_1 = X_1 - \hat{X}_1 \\ e_2 = X_2 - \hat{X}_2 \end{cases} \tag{12}$$

Then, we have:

$$\begin{cases} \dot{e}_1 = \dot{X}_1 - \dot{\hat{X}}_1 \\ \dot{e}_2 = \dot{X}_2 - \dot{\hat{X}}_2 \end{cases}$$

$$\begin{cases} \dot{e}_1 = (A_1 - S_{\alpha 1}^{-1} C^T C)\, e_1 + g_1 - \hat{g}_1 \\ \dot{e}_2 = (A_2 - S_{\alpha 2}^{-1} C^T C)\, e_2 + g_2 - \hat{g}_2 \end{cases} \tag{13}$$

Equation (13) with parameter uncertainties in the DFIG-WT was next considered:

$$\begin{cases} \dot{e}_1 = (A_1 - S_{\alpha 1}^{-1} C^T C) e_1 + g_1 - \hat{g}_1 + \Delta A_1 X_1 + \Delta g_1 \\ \dot{e}_2 = (A_2 - S_{\alpha 2}^{-1} C^T C) e_2 + g_2 - \hat{g}_2 + \Delta A_2 X_2 + \Delta g_2 \end{cases} \tag{14}$$

where the terms ΔA_1, ΔA_2, Δg_1 and Δg_2 represent the uncertain terms of A_1, A_2, g_1 and g_2, respectively.

Assumption 2:

The uncertain terms satisfy the following inequalities: $\|\Delta A_1\| \leq \mu_1$, $\|\Delta A_2\| \leq \mu_2$, $\|\Delta g_1\| \leq \mu_3$ and $\|\Delta g_2\| \leq \mu_4$ with $\mu_i > 0$, for $i \in \{1,2,3,4\}$.

This assumption is supported by the fact that the machine parameters are known with a certain degree of precision and are bound, as well as the fact that the machine states are bounded.

Theorem 1. *Subsystems* (10) *and* (11) *are exponential observers for subsystems* (8) *and* (9)*, respectively, for appropriate choices of* α_1 *and* α_2.

Proof. Let us define $V = V_1 + V_2$ as a Lyapunov function. where V_1 and V_2 are the Lyapunov functions for subsystems (10) and (11), respectively, where $V_1 = {e_1}^T S_{\alpha_1} e_1$ and $V_2 = {e_2}^T S_{\alpha_2} e_2$, so:

$$V = {e_1}^T S_{\alpha 1} e_1 + {e_2}^T S_{\alpha 2} e_2 \tag{15}$$

$$\dot{V} = \dot{{e_1}^T} S_{\alpha 1} e_1 + {e_1}^T \dot{S_{\alpha 1}} e_1 + {e_1}^T S_{\alpha 1} \dot{e_1} + \dot{{e_2}^T} S_{\alpha 2} e_2 + {e_2}^T \dot{S_{\alpha 2}} e_2 + {e_2}^T S_{\alpha 2} \dot{e_2} \tag{16}$$

$$\dot{V} = \left(\left(A_1 - S_{\alpha_1}^{-1} C^T C\right) e_1 + g_1 - \hat{g}_1 + \Delta A_1 X_1 + \Delta g_1\right)^T S_{\alpha_1} e_1 + {e_1}^T S_{\alpha_1} \left(\left(A_1 - S_{\alpha_1}^{-1} C^T C\right) e_1 + g_1 - \hat{g}_1 + \Delta A_1 X_1 + \Delta g_1\right) + \left(\left(A_2 - S_{\alpha_2}^{-1} C^T C\right) e_2 + g_2 - \hat{g}_2 + \Delta A_2 X_2 + \Delta g_2\right)^T S_{\alpha_2} e_2 + {e_2}^T S_{\alpha_2} \left(\left(A_2 - S_{\alpha_2}^{-1} C^T C\right) e_2 + g_2 - \hat{g}_2 + \Delta A_2 X_2 + \Delta g_2\right)$$

$$\dot{V} = 2{e_1}^T S_{\alpha_1} \left(A_1 - S_{\alpha_1}^{-1} C^T C\right) e_1 + 2{e_1}^T S_{\alpha_1} (g_1 - \hat{g}_1 + \Delta A_1 X_1 + \Delta g_1) + 2{e_2}^T S_{\alpha_2} \left(A_2 - S_{\alpha_2}^{-1} C^T C\right) e_2 + 2{e_2}^T S_{\alpha_2} \left(g_2 - \hat{g}_2 + \Delta A_2 X_2 + \Delta g_2\right)$$

$$\dot{V} = 2{e_1}^T \left(S_{\alpha_1} A_1 - C^T C\right) e_1 + 2{e_1}^T S_{\alpha_1} (g_1 - \hat{g}_1 + \Delta A_1 X_1 + \Delta g_1) + 2{e_2}^T \left(S_{\alpha_2} A_2 - C^T C\right) e_2 + 2{e_2}^T S_{\alpha_2} \left(g_2 - \hat{g}_2 + \Delta A_2 X_2 + \Delta g_2\right)$$

$$\dot{V} = {e_1}^T \left(-\alpha_1 S_{\alpha_1} + C^T C - 2C^T C\right) e_1 + 2{e_1}^T S_{\alpha_1} (g_1 - \hat{g}_1 + \Delta A_1 X_1 + \Delta g_1) + {e_2}^T \left(-\alpha_2 S_{\alpha_2} + C^T C - 2C^T C\right) e_2 + 2{e_2}^T S_{\alpha_2} \left(g_2 - \hat{g}_2 + \Delta A_2 X_2 + \Delta g_2\right)$$

$$\dot{V} = -{e_1}^T \left(\alpha_1 S_{\alpha_1} + C^T C\right) e_1 + 2{e_1}^T S_{\alpha_1} (g_1 - \hat{g}_1 + \Delta A_1 X_1 + \Delta g_1) - {e_2}^T \left(\alpha_2 S_{\alpha_2} + C^T C\right) e_2 + 2{e_2}^T S_{\alpha_2} \left(g_2 - \hat{g}_2 + \Delta A_2 X_2 + \Delta g_2\right)$$

$$\dot{V} = -\alpha_1 V_1 - {e_1}^T C^T C e_1 + 2{e_1}^T S_{\alpha 1} (g_1 - \hat{g}_1 + \Delta A_1 X_1 + \Delta g_1) - \alpha_2 V_2 - {e_2}^T C^T C e_2 + 2{e_2}^T S_{\alpha_2} \left(g_2 - \hat{g}_2 + \Delta A_2 X_2 + \Delta g_2\right) \tag{17}$$

Using Assumption 1, we have:

$$\begin{cases} k_{min}(S_{\alpha 1}) \leq \|S_{\alpha 1}\| \leq k_{max}(S_{\alpha 1}); l_{min}(S_{\alpha 2}) \leq \|S_{\alpha 2}\| \leq l_{max}(S_{\alpha 2}) \\ \|g_1 - \hat{g}_1\| \leq \gamma_1 \|e_1\| \;;\; \|g_2 - \hat{g}_2\| \leq \gamma_2 \|e_2\| \\ \|X_1\| \leq \gamma_3 \;;\; \|X_2\| \leq \gamma_4 \end{cases} \tag{18}$$

$k_{min}, l_{min}, k_{max}$ and l_{max} are the minimal and maximal eigenvalues S_{α_1} and S_{α_2}, respectively. γ_i, $i \in \{1,2,3,4\}$ is a positive constant.

Along with $C^T C > 0$, we can write:

$$\dot{V} \leq -\alpha_1 V_1 + 2\|e_1\| \|S_{\alpha_1}\| \|g_1 - \hat{g}_1 + \Delta A_1 X_1 + \Delta g_1\| - \alpha_2 V_2 + 2\|e_1\| \|S_{\alpha_2}\| \|g_2 - \hat{g}_2 + \Delta A_2 X_2 + \Delta g_2\|$$

$$\dot{V} \leq -\alpha_1 V_1 + 2\gamma_1 \|S_{\alpha_1}\| \|e_1\|^2 + 2\mu_1 \gamma_3 \|S_{\alpha_1}\| \|e_1\| + 2\mu_3 \|S_{\alpha_1}\| \|e_1\| - \alpha_2 V_2 + 2\gamma_2 \|S_{\alpha_2}\| \|e_2\|^2 + 2\mu_2 \gamma_4 \|S_{\alpha_2}\| \|e_2\| + 2\mu_4 \|S_{\alpha_2}\| \|e_2\|$$

$$\dot{V} \leq (2\gamma_1 - \alpha_1) V_1 + 2(\mu_1 \gamma_3 + \mu_3) k_{max}(S_{\alpha_1}) \|e_1\| + (2\gamma_2 - \alpha_2) V_2 + 2(\mu_2 \gamma_4 + \mu_4) l_{max}(S_{\alpha_2}) \|e_2\| \tag{19}$$

Consider now that:

$$\begin{cases} k_{min}(S_{\alpha_1}) \leq \|S_{\alpha_1}\| \leq k_{max}(S_{\alpha_1}) \\ l_{min}(S_{\alpha_2}) \leq \|S_{\alpha_2}\| \leq l_{max}(S_{\alpha_2}) \end{cases}$$

$$\Rightarrow \begin{cases} k_{min}(S_{\alpha_1}) \|e_1\|^2 \leq \|S_{\alpha_1}\| \|e_1\|^2 \leq k_{max}(S_{\alpha_1}) \|e_1\|^2 \\ l_{min}(S_{\alpha_2}) \|e_2\|^2 \leq \|S_{\alpha_2}\| \|e_2\|^2 \leq l_{max}(S_{\alpha_2}) \|e_2\|^2 \end{cases}$$

$$\Rightarrow \begin{cases} \sqrt{k_{min}(S_{\alpha_1})} \|e_1\| \leq \sqrt{V_1} \leq \sqrt{k_{max}(S_{\alpha_1})} \|e_1\| \\ \sqrt{l_{min}(S_{\alpha_2})} \|e_2\| \leq \sqrt{V_2} \leq \sqrt{l_{max}(S_{\alpha_2})} \|e_2\| \end{cases}$$

$$\Rightarrow \begin{cases} \|e_1\| \leq \frac{1}{\sqrt{k_{min}(S_{\alpha_1})}}\sqrt{V_1} \\ \|e_2\| \leq \frac{1}{\sqrt{l_{min}(S_{\alpha_2})}}\sqrt{V_2} \end{cases} \tag{20}$$

Substituting (20) into (19):

$$\dot{V} \leq -(\alpha_1 - 2\gamma_1) V_1 + 2(\mu_1\gamma_3 + \mu_3) \frac{k_{max}(S_{\alpha_1})}{\sqrt{k_{min}(S_{\alpha_1})}}\sqrt{V_1} - (\alpha_2 - 2\gamma_2) V_2 + 2(\mu_2\gamma_4 + \mu_4) \frac{l_{max}(S_{\alpha_2})}{\sqrt{l_{min}(S_{\alpha_2})}}\sqrt{V_2}$$

$$\dot{V} \leq -(\alpha_1 - \vartheta_1) V_1 - (\alpha_2 - \vartheta_2) V_2 + \vartheta_3\sqrt{V_1} + \vartheta_4\sqrt{V_2} \tag{21}$$

with:

$$\vartheta_1 = 2\gamma_1;\ \vartheta_2 = 2\gamma_2;\ \vartheta_3 = 2(\mu_1\gamma_3 + \mu_3) \frac{k_{max}(S_{\alpha_1})}{\sqrt{k_{min}(S_{\alpha_1})}};$$

$$\vartheta_4 = 2(\mu_2\gamma_4 + \mu_4) \frac{l_{max}(S_{\alpha_2})}{\sqrt{l_{min}(S_{\alpha_2})}}$$

We pose:

$$\begin{cases} \varepsilon_1 = min\{\alpha_1 - \vartheta_1, \alpha_2 - \vartheta_2\} \\ \varepsilon_2 = max\{\vartheta_3, \vartheta_4\} \end{cases}$$

where $\alpha_1 > \vartheta_1$; $\alpha_1 > \vartheta_1$ and using: $\sqrt{V_1} + \sqrt{V_2} \leq \sqrt{V}$ Equation (21) becomes:

$$\dot{V} \leq -\varepsilon_1 V + \varepsilon_2\sqrt{V}$$

Thus, we have two cases:

1) The parameters of the machine are known ($\varepsilon_2 = 0$), so we need just to choose: $\alpha_1 > \vartheta_1$; $\alpha_1 > \vartheta_1$
2) The parameters of the machine with uncertainties ($\varepsilon_2 \neq 0$), in this case, mean that:

$$\dot{V} \leq -(1-\epsilon)\varepsilon_1 V - \epsilon\varepsilon_1 V + \varepsilon_2\sqrt{V},\ \ 0 < \varepsilon < 1$$

$$\Rightarrow \dot{V} \leq -(1-\varepsilon)\varepsilon_1 V \qquad \forall \|e\| \geq \frac{\varepsilon_2}{\epsilon\varepsilon_1}$$

Therefore, it is required that the estimation error be always $\|e\| \geq \frac{\varepsilon_2}{\epsilon\varepsilon_1}$, and this condition can be reached by adjusting ε_1. □

4. HIGH-ORDER SLIDING MODE CONTROL DESIGN

In this section, we present the super twisting-based HOSM (ST-HOSM) for the control of DFIG-WT in the stationary frame; the super twisting algorithm is used here to overcome the issue of chattering.

The objective of this control design was to control the electromagnetic torque and reactive power. Therefore, the sliding surfaces are chosen as follows:

$$S = \begin{bmatrix} S_1 \\ S_2 \end{bmatrix} = \begin{bmatrix} {T_{em}}^* - T_{em} \\ {Q_s}^* - Q_s \end{bmatrix} \tag{22}$$

When the system states attain and remain on the sliding surface, $S = \dot{S} = 0$.

Its derivative is written as [54]:

$$\dot{S} = \begin{bmatrix} -\dot{T}_{em} \\ -\dot{Q}_s \end{bmatrix} \tag{23}$$

The relation between the electromagnetic torque and the stator active power can be represented by [53]:

$$T_{em} = \frac{p}{\omega_s} P_s \tag{24}$$

Then:

$$\dot{S} = \begin{bmatrix} -1.5(p/\omega_s)(v_{s\alpha}\dot{l_{s\alpha}} + \dot{v_{s\alpha}} i_{s\alpha} + v_{s\beta}\dot{l_{s\beta}} + \dot{v_{s\beta}} i_{s\beta}) \\ -1.5\left(\dot{v_{s\beta}} i_{s\alpha} + v_{s\beta}\dot{l_{s\alpha}} - \dot{v_{s\alpha}} i_{s\beta} - \dot{v_{s\alpha}} i_{s\beta}\right) \end{bmatrix} \tag{25}$$

with: $\dot{v_{s\alpha}}=\omega_s v_{s\beta}$; $\dot{v_{s\beta}}=-\omega_s v_{s\alpha}$

$$\dot{S} = \frac{1.5L_m}{L_r L_s \sigma} \begin{bmatrix} (p/\omega_s)v_{s\alpha} & (p/\omega_s)v_{s\beta} \\ v_{s\beta} & -v_{s\alpha} \end{bmatrix} \begin{bmatrix} v_{r\alpha} \\ v_{r\beta} \end{bmatrix}$$

$$-\frac{1.5p}{L_s\sigma\omega_s} \begin{bmatrix} 1 & 1 \\ 0 & 0 \end{bmatrix} \begin{bmatrix} {v_{s\alpha}}^2 \\ {v_{s\beta}}^2 \end{bmatrix} - \frac{1.5L_m}{L_r L_s \sigma}$$

$$\begin{bmatrix} (p/\omega_s)\,L_m(R_r v_{s\alpha} - p\Omega_m L_r v_{s\beta}) & (p/\omega_s)L_m(R_r v_{s\beta} + p\Omega_m L_r v_{s\alpha}) \\ L_m(p\Omega_m L_r v_{s\alpha} + R_r v_{s\beta}) & L_m(p\Omega_m L_r v_{s\beta} - R_r v_{s\alpha}) \end{bmatrix} \begin{bmatrix} i_{r\alpha} \\ i_{r\beta} \end{bmatrix}$$

$$-\frac{1}{L_r L_s \sigma} \begin{bmatrix} -R_s L_r & \left(L_r L_s \sigma p - \Omega_m p^2 {L_m}^2 \omega_s\right) \\ \left(\Omega_m {L_m}^2 \omega_s - L_r L_s \sigma {\omega_s}^2/p\right) & -R_s L_r \end{bmatrix} \begin{bmatrix} T_{em} \\ Q_s \end{bmatrix} \tag{26}$$

Equation (10) can be rewritten in canonical form:

$$\dot{S} = GV + F \tag{27}$$

where

$$G = \frac{1.5L_m}{L_r L_s \sigma} \begin{bmatrix} (p/\omega_s)\,v_{s\alpha} & (p/\omega_s)\,v_{s\beta} \\ v_{s\beta} & -v_{s\alpha} \end{bmatrix};\ V = \begin{bmatrix} v_{r\alpha} \\ v_{r\beta} \end{bmatrix}$$

$$F = -\frac{1.5p}{L_s\sigma\omega_s} \begin{bmatrix} 1 & 1 \\ 0 & 0 \end{bmatrix} \begin{bmatrix} {v_{s\alpha}}^2 \\ {v_{s\beta}}^2 \end{bmatrix} - \frac{1.5L_m}{L_r L_s \sigma}$$

$$\begin{bmatrix} (p/\omega_s)\,L_m(R_r v_{s\alpha} - p\Omega_m L_r v_{s\beta}) & (p/\omega_s)L_m(R_r v_{s\beta} + p\Omega_m L_r v_{s\alpha}) \\ L_m(p\Omega_m L_r v_{s\alpha} + R_r v_{s\beta}) & L_m(p\Omega_m L_r v_{s\beta} - R_r v_{s\alpha}) \end{bmatrix} \begin{bmatrix} i_{r\alpha} \\ i_{r\beta} \end{bmatrix}$$

$$-\frac{1}{L_r L_s \sigma} \begin{bmatrix} -R_s L_r & \left(L_r L_s \sigma p - \Omega_m p^2 {L_m}^2 \omega_s\right) \\ \left(\Omega_m {L_m}^2 \omega_s - L_r L_s \sigma {\omega_s}^2/p\right) & -R_s L_r \end{bmatrix} \begin{bmatrix} T_{em} \\ Q_s \end{bmatrix}$$

The control law is defined as:

$$V = V_e + V_s \tag{28}$$

V_e represents the equivalent control, and it can be obtained from:

$$\dot{S} = 0 \Rightarrow V = -G^{-1}F$$

V_s is the switching control obtained from the super twisting algorithm [21], [54]:

$$V_e = -G^{-1} \begin{bmatrix} \int A_1 sign(S_1) + B_1 |S_1|^{1/2} sign(S_1) \\ \int A_2 sign(S_2) + B_2 |S_2|^{1/2} sign(S_2) \end{bmatrix} \tag{29}$$

The corresponding sufficient conditions for finite-time convergence to the sliding manifold are:

$$\begin{cases} B_1 > \frac{\phi_1}{\Gamma_{m1}};\ {A_1}^2 \geq \frac{4\ \phi_1\ \Gamma_{M1}\ (B_1 + \phi_1)}{{\Gamma_{m1}}^3 (B_1 - \phi_1)} \\ B_2 > \frac{\phi_2}{\Gamma_{m2}};\ {A_2}^2 \geq \frac{4\ \phi_2\ \Gamma_{M2}\ (B_2 + \phi_2)}{{\Gamma_{m2}}^3 (B_2 - \phi_2)} \end{cases}$$

with:

$$\begin{cases} |G_1| < \phi_1;\ 0 < \Gamma_{m1} \leq F_1 \leq \Gamma_{M1} \\ |G_2| < \phi_2;\ 0 < \Gamma_{m2} \leq F_2 \leq \Gamma_{M2} \end{cases}$$

where Γ_{m1}, Γ_{m2}, Γ_{M1}, Γ_{M2}, ϕ_1 and ϕ_2 are positive constants.

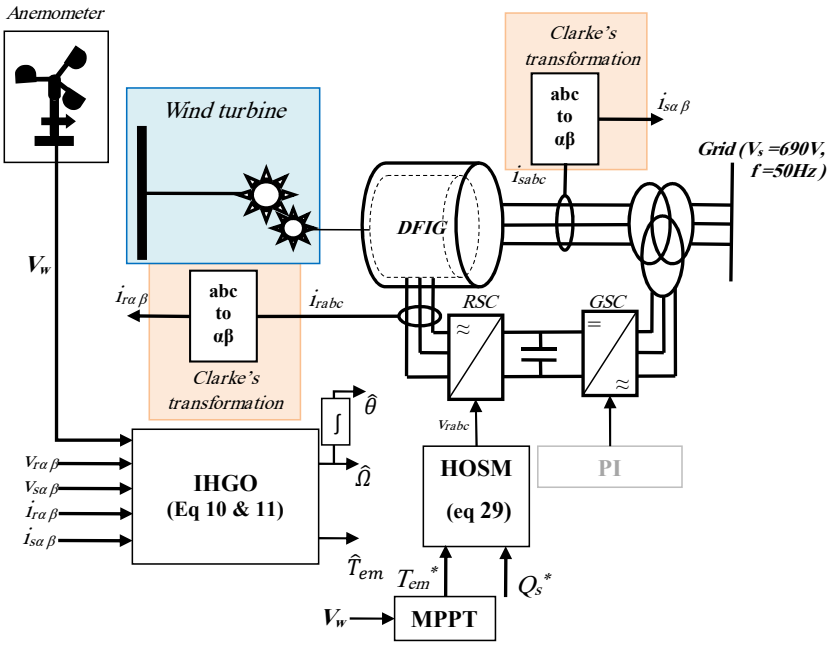

Fig. 4. Configuration of the simulated power system

5. Simulation Results and Discussion

Simulations were conducted to illustrate the effectiveness of the proposed observer and control strategy for a connected DFIG-WT. The wind power generator shown in Fig. 4 was connected to a three-phase system with a voltage of 690 Vrms and a frequency of 50 Hz. The system's main parameter values are listed in Table 1 [55]. Table 2 displays the control parameters of the proposed ST-HOSM and observer. The observer's gains were selected to ensure faster convergence than the controller. The simulation time step was set to 5 μs, and the switching frequency of the proposed control strategy was fixed at 4 kHz. The performance of the proposed strategy is investigated by considering two cases:

Case 1: *open loop system*

- Verify the observer without the controller

Case 2: *controller associated with the observer*

- Scenario 1: normal conditions
- Scenario 2: active power variation and speed variation
- Scenario 3: power grid terminal voltage drop fault
- Scenario 4: robustness test
- Scenario 5: rotor current sensor fault

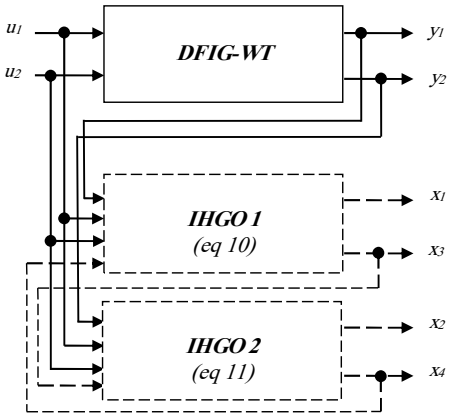

Fig. 5. Speed and electromagnetic torque IHGOs

5.1. Case 1: *open loop system*

First, the DFIG-WT was excited through the rotor voltage (V_r = 50 V) to test the IHGO (Fig. 5) without the controller (open loop system).

The initial state conditions are set as follows:

DFIG-WT:

$$X_1(0) = [36.164\ A; 157.58\ rad/s]^T\ ,$$

$$X_2\ (0) = \ [-622.87\ A; -3247.575\ N.m]^T$$

IHGO:

$$\hat{X}_1(0) = [200\ A; 140\ rad/s]^T\ , \hat{X}_2(0) = [-1400\ A; -5000\, N.m]^T$$

The wind profile used for simulation is presented in Fig. 6 during 10 s.

Both observers were given equal gains. In order to demonstrate the performance of the observer, we examined three different

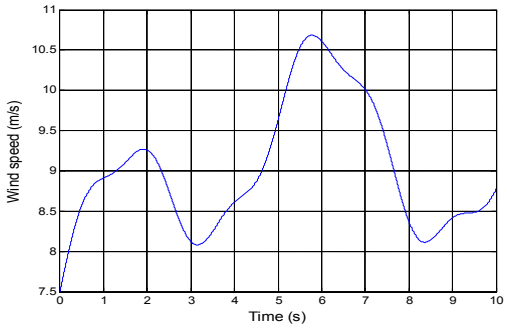

Fig. 6. Wind speed profile

Table 1. Turbine and generator parameters

Generator parameter	Value	Turbine parameter	Value
P_{rated}	$2MW$	R	$42m$
R_s	0.026Ω	ρ	$1.225kg/m^3$
R_r	0.029Ω	G	100
L_s	$0.026H$	J	$90kg.m^2$
L_r	$0.026\ H$	f_v	10^{-3}
L_m	$0.025H$		
V_s	$690V$		
f	$50Hz$		
V_{bus}	$1150V$		
p	2		

Table 2. Turbine and generator parameters

Observer Gains	Controller Gains
$\alpha_1 = \alpha_2 = 10000$	$A_1 = 10^6; B_1 = 10^7; A_2 = 4 * 10^6; B_2 = 10^7$

values for the observer gain. The tracking curves of the measured and estimated values of the rotor current in the α-axis and β-axis, as well as the speed, angle, and electromagnetic torque, are presented in Figures 7 and 8. As depicted, the convergence time is highly dependent on the observer gain, with a small convergence time indicating a larger gain. However, an excessively large gain may result in highly sensitive and noisy estimations.

5.2. Case 2: *controller associated with the observer*

Several numerical simulations were conducted to evaluate the performance of the controller and observer. Specifically, the wind speed profile was maintained consistently across all simulation runs in order to ensure a fair and consistent comparison of the controller's performance (see Figure 6).

- Scenario 1: normal conditions.

In this scenario, the system is simulated under nominal parameters. The rotor speed, rotor angle, and electromagnetic torque are provided by the observer. The proposed control scheme is compared to conventional Super-twisting based HOSM (CST) in the *dq* frame studied in [21] and field-oriented control (PI).

Fig. 9 presents the rotor speed (a), electromagnetic torque (b), reactive power (c), and active power (d). It can be seen that the variables track their references. The proposed control approach exhibits good reference tracking, low chatter, and low torque ripple. The observer estimation errors shown in Fig. 9 (e-f) are very small. The errors are calculated between the real rotor speed ω and its estimation ω_{es} (e) and between the real electromagnetic torque Tem and its estimation Tem$_{es}$ (f).

Fig. 10 depicts the three-phase stator current and rotor current of the proposed control strategy and CST. When the generator operates nearly at synchronous speed, the rotor current loses its sinusoidal shape at 1.6 s, 2.1 s, 4.7 s, and 7.5 s, as shown in Fig. 10 (b). The proposed control strategy reduces the harmonics in the rotor current, as shown in Fig. 11.

- Scenario 2: active power variation and speed variation

We perform more simulations to examine the dynamic behavior of the observer and controller in different operating modes. The rotor speed is varied from subsynchronous to synchronous and then supersynchronous, as shown in Fig. 12 (a). In all operating modes, the observer provides accurate estimations of electromagnetic torque (Fig. 12 (f)) and rotor speed (Fig. 12 (e)). Furthermore, the proposed control strategy presents a fast response time without overshooting and good tracking of references compared to PI and CST.

Next, we test the stability of the proposed strategy under active power variation. Variable steps are used as a reference diagram of the active power to assess the observer accuracy and control strategy tracking performance (Fig. 13 (d)). In Fig. 13, the estimation of rotor and electromagnetic torque follows their actual variables. The reactive power is kept at 0 VAR to ensure a unity power factor. The controller responses track their references perfectly. The proposed strategy shows good transient performance. Additionally, we can notice that the strategy guarantees decoupled power control (Fig. 13 (c)).

- Scenario 3: power grid terminal voltage fault.

According to the grid code, the WECS is required to maintain the connection to the power grid during and after the voltage drop.

To test the FRT capability of the controller+observer, three grid fault were proposed:

1) Symmetrical voltage dip:
   - three-phase grid voltage dip of 50% amplitude occurred at 3.7 s and was restored at 3.9 s (Fig. 14),
2) Asymmetry in voltage dip:
   - a 50% amplitude two-phase grid voltage dip occurred from 3.7 s to 3.9 s (Fig. 17);
   - A 50% amplitude one-phase grid voltage dip occurred from 3.7 s to 3.9 s (Fig. 20).

The results of the conducted tests demonstrate the effectiveness of the proposed controller and observer for mitigating the impact of grid voltage faults on wind turbines. Fig. 15 shows the response of the system when a symmetrical grid voltage dip occurs, revealing the changes in rotor speed, electromagnetic torque, reactive power, and active power. Figs. 18 and 21 illustrate the responses of the rotor speed, the electromagnetic torque, the reactive power and the active power when the grid voltage is temporarily reduced during 200 ms for two- and one-phase voltage dips, respectively. The results indicate that the controller+ observer can effectively maintain wind power extraction during the fault. Moreover, the electromagnetic torque, reactive power, and active power rapidly return to their references once the fault is cleared, indicating a good recovery time. The observer preserves its performance for all scenarios of grid voltage faults, and the asymmetrical voltage dips do not affect the estimation process.

Figs. 16, 19, and 22 demonstrate the response of the system to three-phase, two-phase, and one-phase voltage dips, respectively, by presenting the stator and rotor currents. The results indicate that the proposed controller and observer are capable of holding current levels within acceptable bounds during transient events.

Nevertheless, protection must be implemented to protect the power converter using the crowbar at the beginning of the fault.

- Scenario 4: robustness test

The generator resistances were modified ($R'_s = 1.5 * R_s$, $R'_r = 1.5 * R_r$) to assess the controllers under uncertain parameters. R_s and R_r are the nominal values of the stator and rotor resistance illustrated in Table 1. The variables of the proposed control strategy and PI presented in Fig. 23 tracked their references perfectly. However, the CST controller began to lose control when the wind speed was high. The observer accurately estimates the electromagnetic torque and the speed even in the presence of parameter uncertainties.

- Scenario 5: rotor current sensor fault.

Sensor measurement noise is an unfavorable condition that can impact the results. To address this issue, Gaussian noise was added to the current measurements (as shown in Fig. 24), and further simulations were performed. The results, as presented in Fig. 25 and Fig. 26, show the rotor speed (a), electromagnetic torque (b), reactive power (c), active power (d), stator and rotor current. Interestingly, the controller+observer was able to maintain its performance and robustness even in the presence of noise.

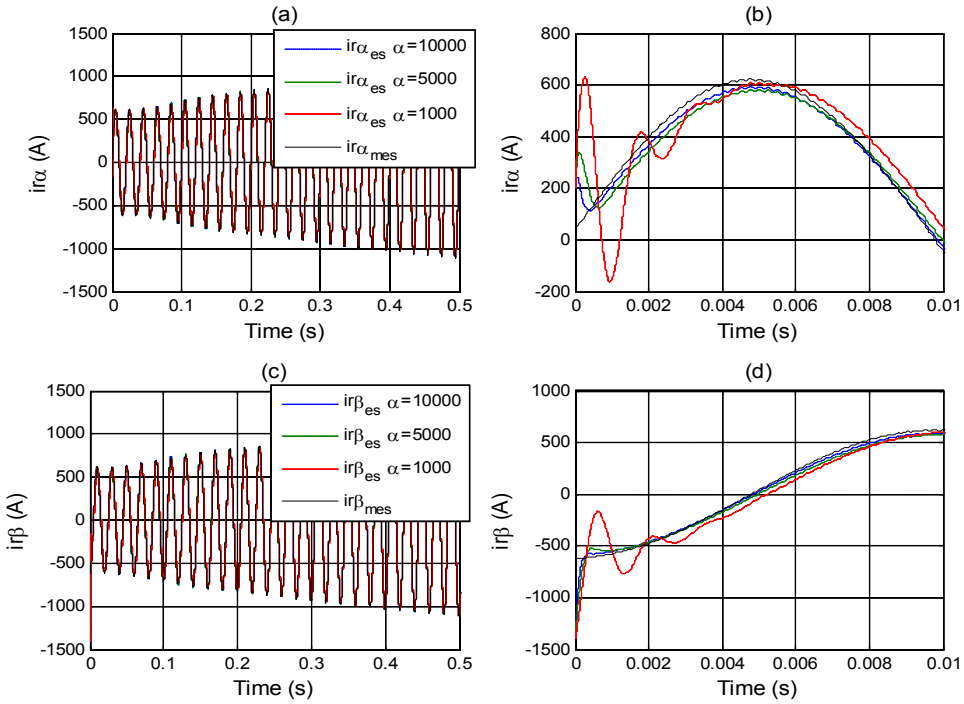

Fig. 7. Measured and estimated rotor current in the stator frame. (Open loop)

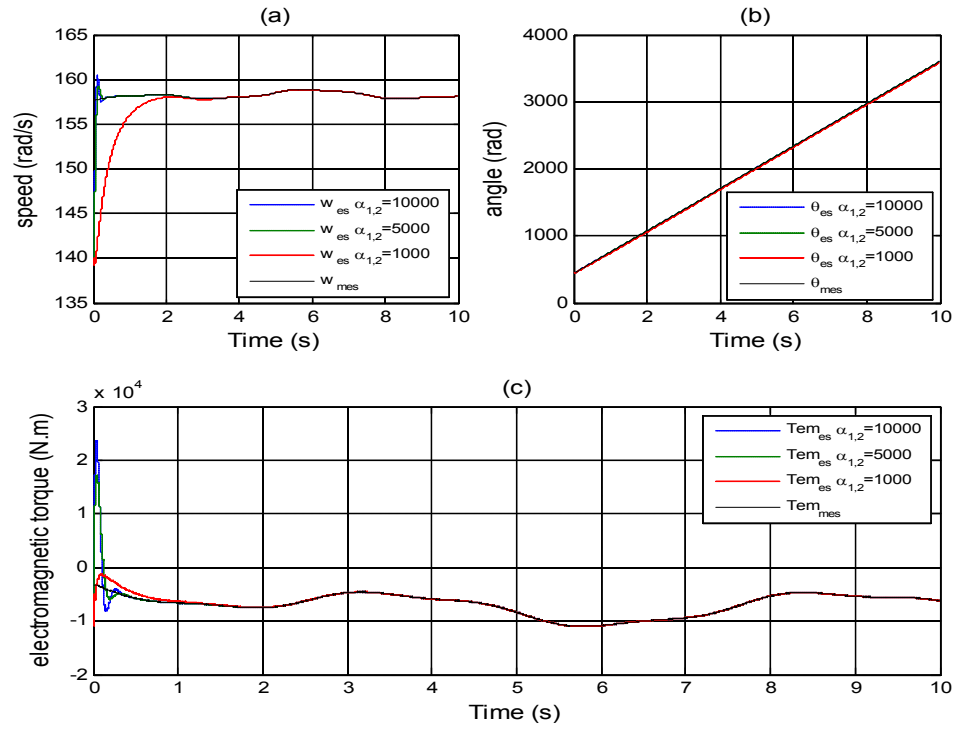

Fig. 8. (a) Speed, (b) angle and (c) electromagnetic torque. (Open loop)

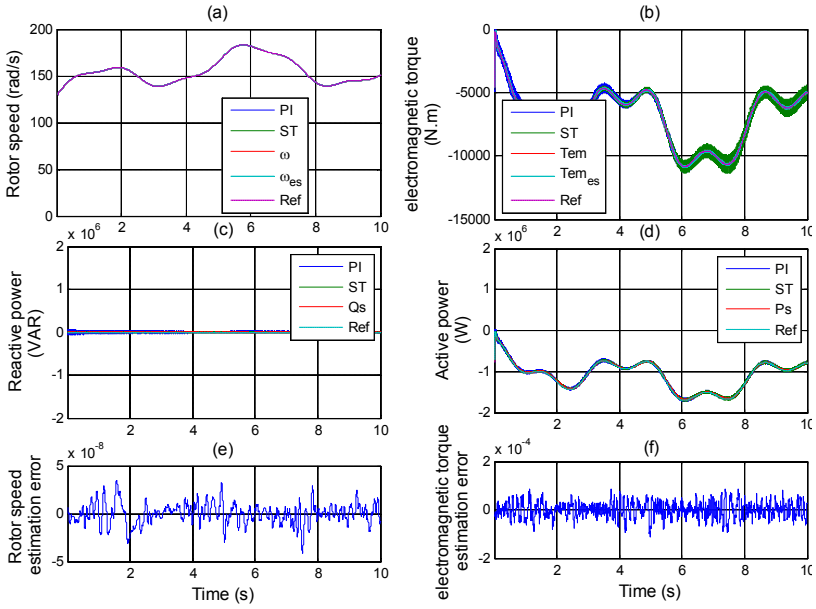

Fig. 9. (a) Rotor speed, (b) electromagnetic torque, (c) reactive power, (d) active power, (e) speed estimation error, (f) electromagnetic torque estimation error. (Normal conditions)

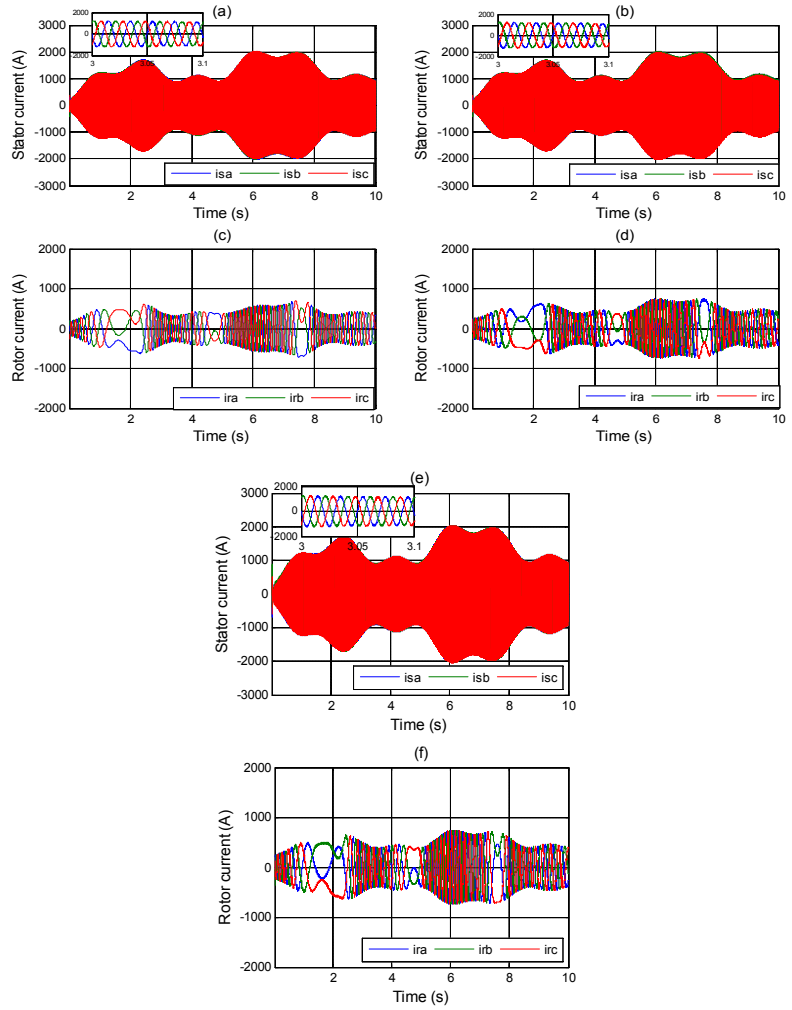

Fig. 10. Stator current: (a) proposed control strategy, (b) CST, (c) PI. Rotor current (a) proposed control strategy, (b) CST, (c) PI. (Normal conditions)

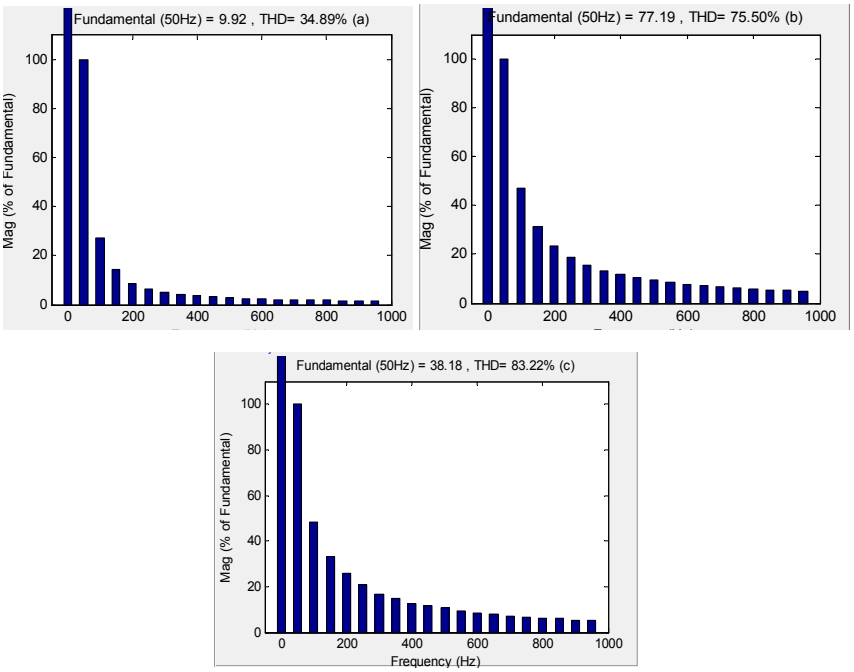

Fig. 11. Harmonic spectrum of rotor current: (a) proposed control strategy, (b) CST, (c) PI

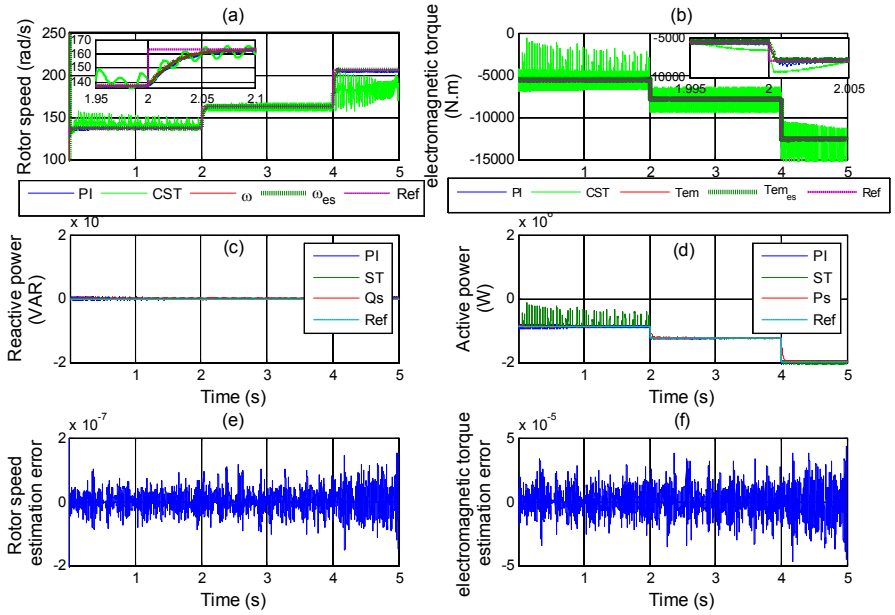

Fig. 12. (a) Rotor speed, (b) electromagnetic torque, (c) reactive power, and (d) active power, (e) speed estimation error, (f) electromagnetic torque estimation error. (Rotor speed variations)

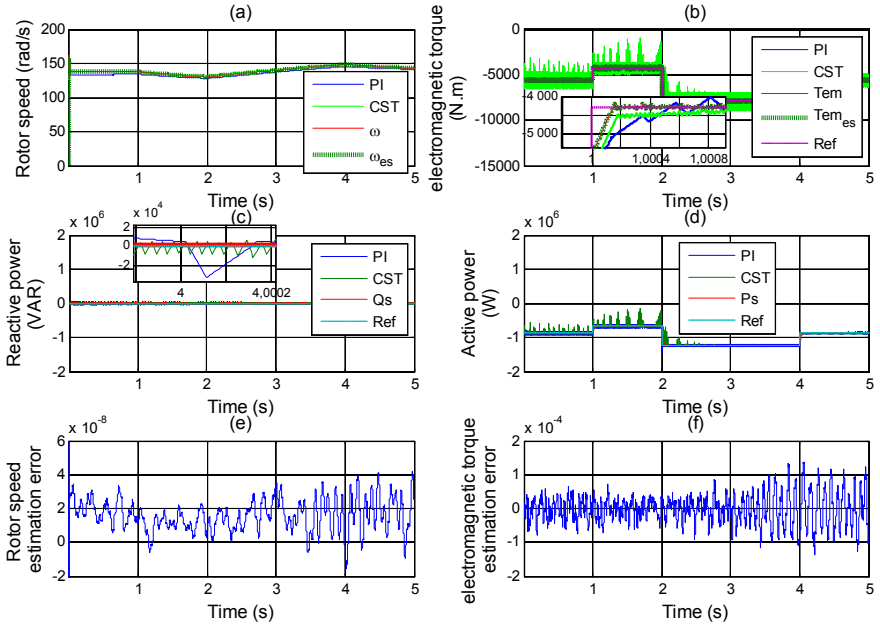

Fig. 13. (a) Rotor speed, (b) electromagnetic torque, (c) reactive power, and (d) active power, (e) speed estimation error, (f) electromagnetic torque estimation error. (Active power variations)

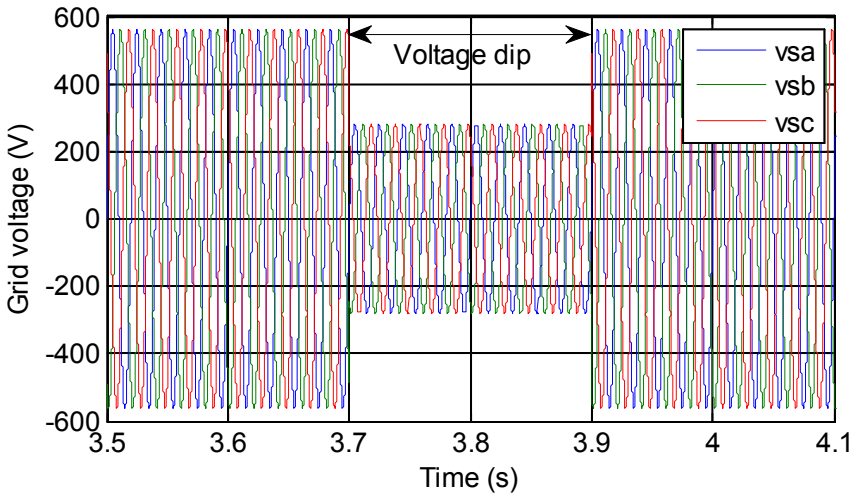

Fig. 14. Three phases grid voltage dip of 50% (between 3.7 s – 3.9 s)

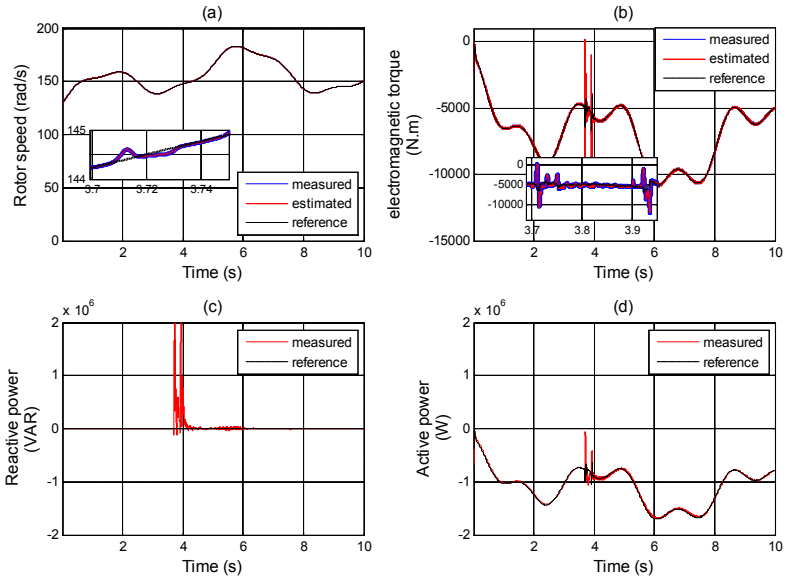

Fig. 15. (a) Rotor speed, (b) electromagnetic torque, (c) reactive power, (d) Active power. (Symmetrical voltage dip)

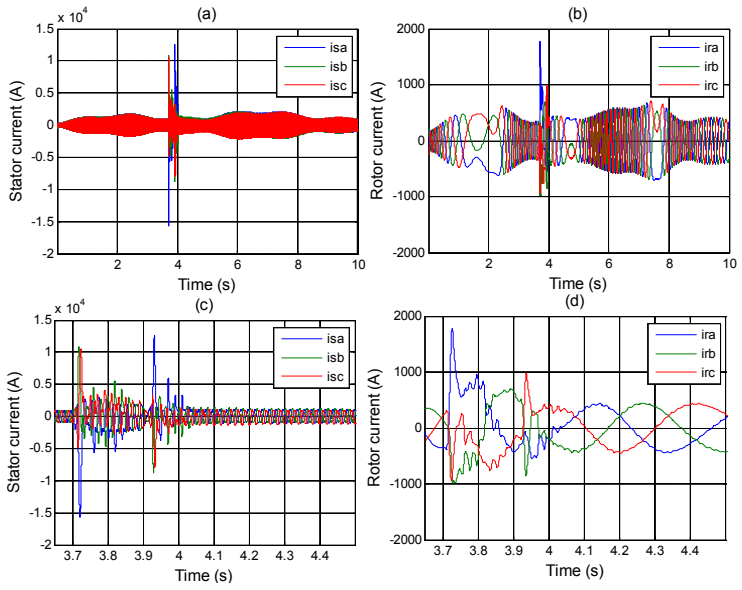

Fig. 16. (a) Stator current and (b) rotor current. (Symmetrical voltage dip)

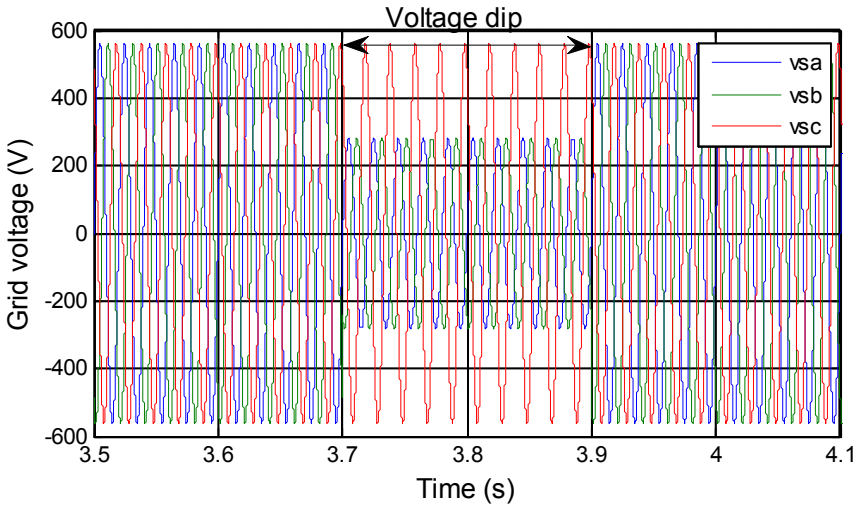

Fig. 17. Two phases grid voltage dip of 50% (between 3.7 s – 3.9 s)

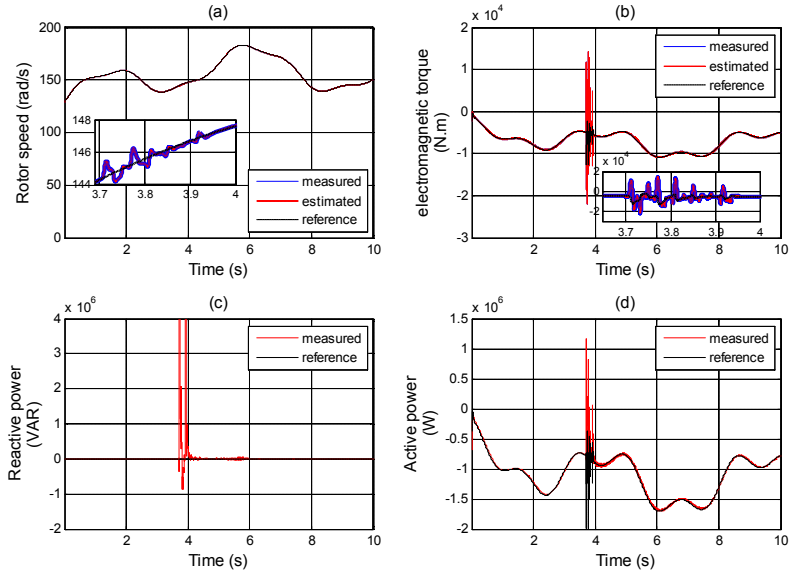

Fig. 18. (a) Rotor speed, (b) electromagnetic torque, (c) reactive power, (d) active power. (Two phases grid voltage dip)

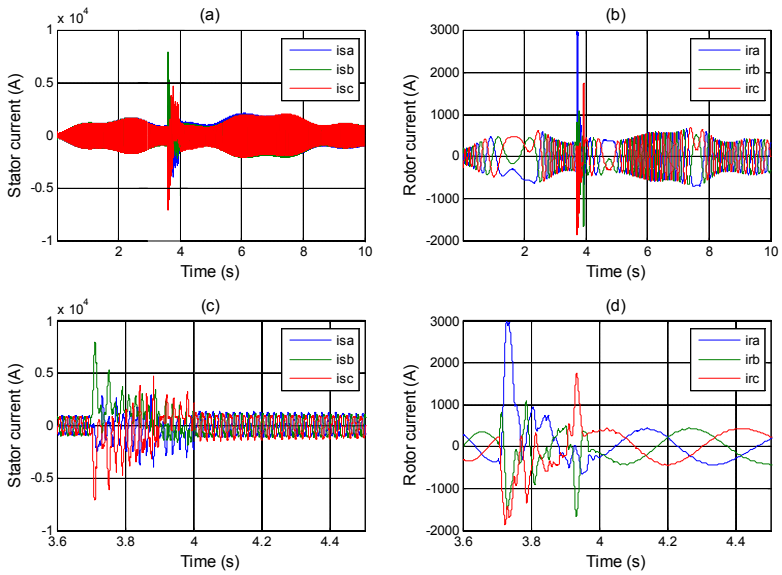

Fig. 19. (a) Stator current and (b) rotor current. (Two phases grid voltage dip)

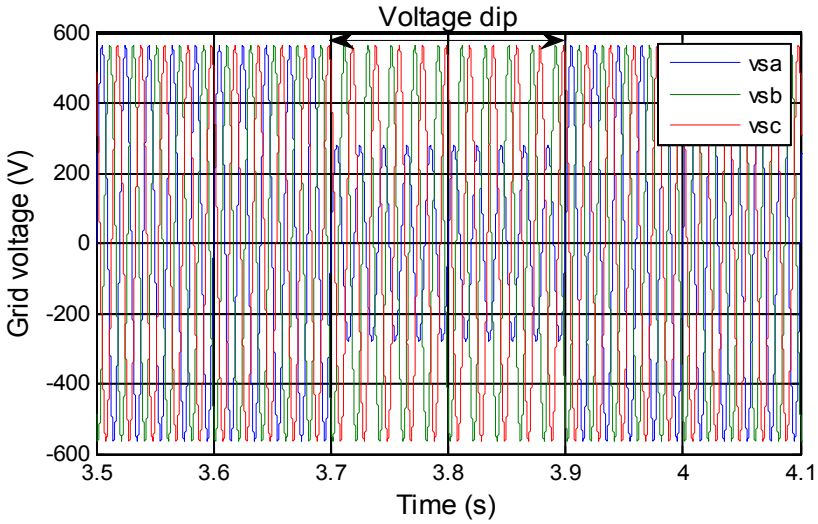

Fig. 20. One phase grid voltage dip of 50% (between 3.7 s – 3.9 s)

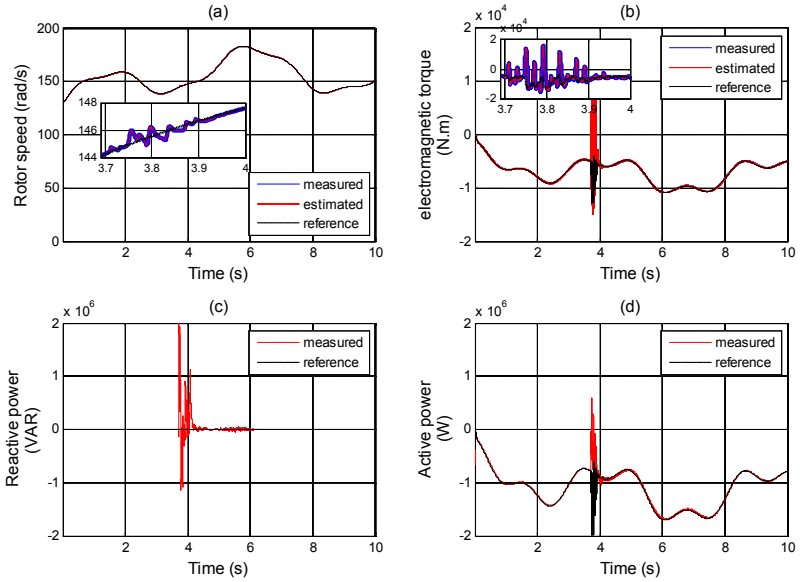

Fig. 21. (a) Rotor speed, (b) electromagnetic torque, (c) reactive power, (d) active power. (One phases grid voltage dip)

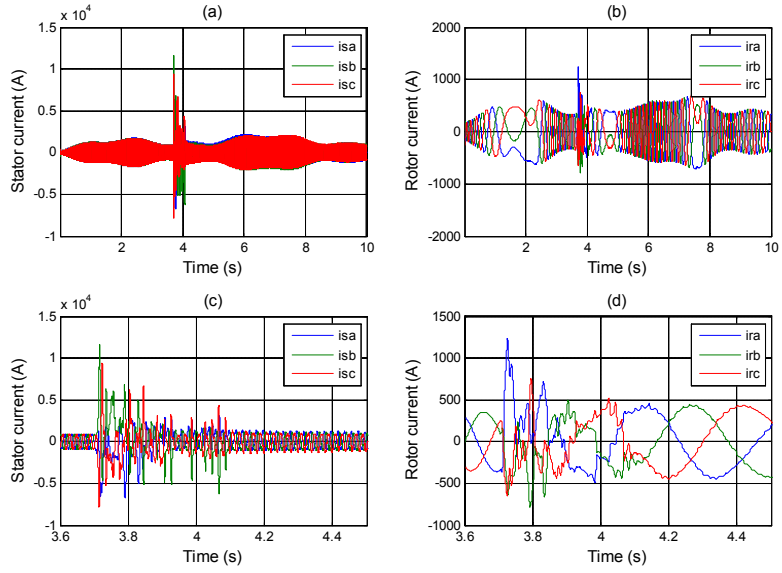

Fig. 22. (a) Stator current and (b) rotor current. (Two phases grid voltage dip)

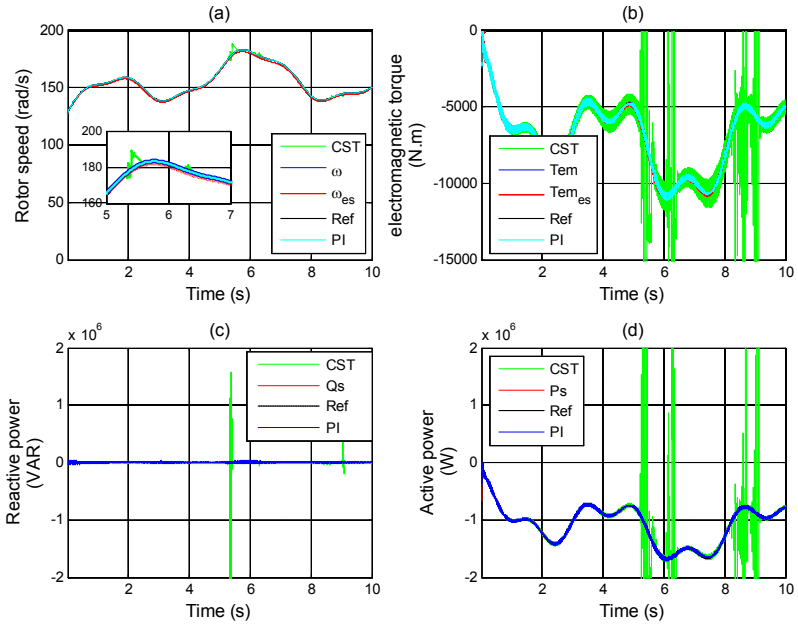

Fig. 23. (a) Rotor speed, (b) electromagnetic torque, (c) reactive power, (d) active power. (One phases grid voltage dip)

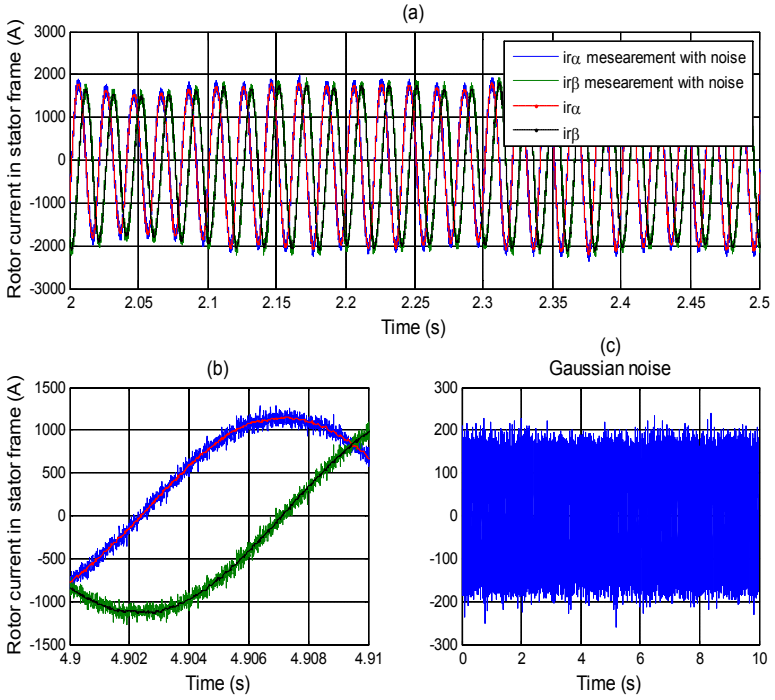

Fig. 24. Rotor current in the stator frame, (b) details and (c) the noise added to the current measurement

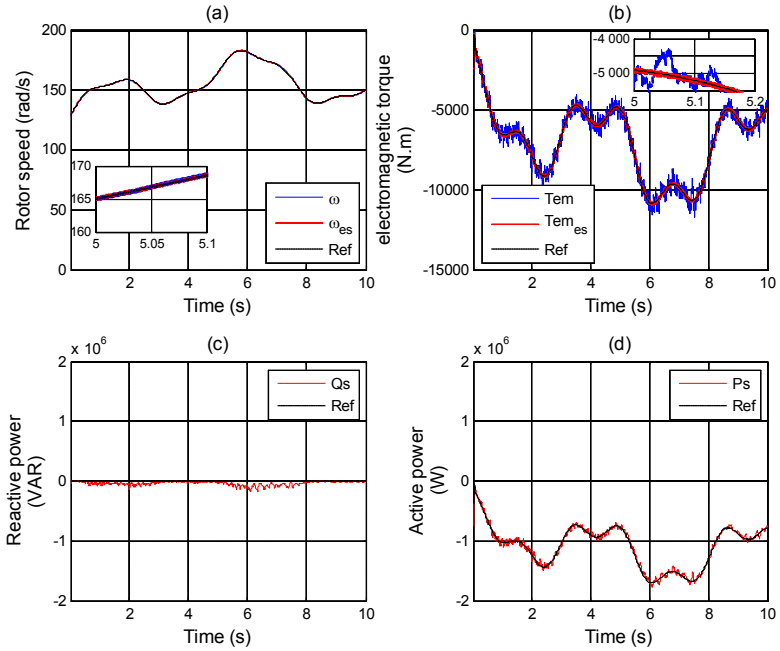

Fig. 25. (a) Rotor speed, (b) electromagnetic torque measured and reference: (c) reactive power, (d) active power. (Sensor fault)

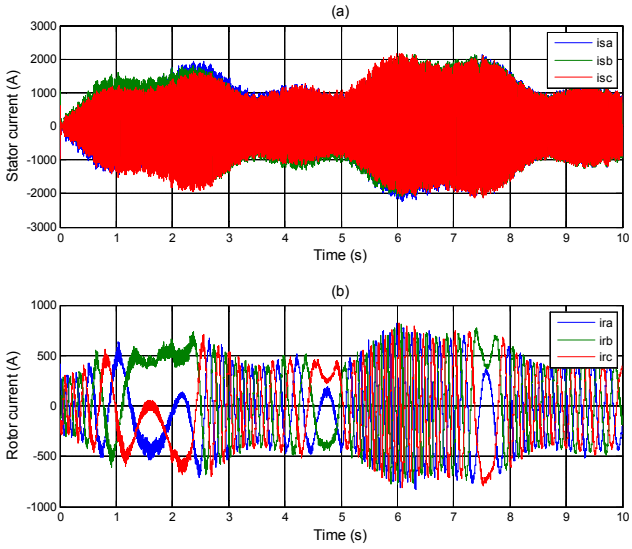

Fig. 26. (a) Stator current and (b) rotor current. (Sensor fault)

The proposed sensorless control strategy was rigorously tested in the presence of internal system uncertainties and external disturbances. The results demonstrate that the variables are able to track their references with high accuracy of the observer estimation. In cases where the DFIG system is particularly sensitive, such as in the event of a grid voltage fault, the controller is able to maintain the current within acceptable levels. Furthermore, the system response is able to quickly recover when the grid voltage returns to normal. The observers for electromagnetic torque and speed showed exceptional accuracy and robustness for the proposed cases.

6. Conclusion

In the current study, we implemented a robust control approach to directly and independently manage the electromagnetic torque and reactive power of DFIG-WTs. The adopted control technique was the ST-HOSM in association with an IHGO. This scheme was implemented in the $\alpha\beta$ frame to avoid the utilization of the PLL. Additionally, the observer was designed to estimate the speed, position, and electromagnetic torque using currents, voltages and wind speed measurements. The observer stability was demonstrated against the parameter variations; hence, the high value gain of the observer assures an accurate estimation even with high speed. Furthermore, an open-loop system fulfills the need for the estimated states' convergence to the real state. The sensorless control strategy was compared to the conventional Super-twisting algorithm and PI. Overall, the results validate the effectiveness of the proposed controller and observer in mitigating the impact of parameter uncertainties, grid voltage faults and current sensor noise.

References

[1] World Wind Energy Association and others,"Worldwide Wind Capacity Reaches 744 Gigawatts – An Unprecedented 93 Gigawatts added in 2020," https://wwindea.org/worldwide-wind-capacity-reaches-744-gigawatts/ (accessed Dec. 12, 2021).

[2] "Vestas–Page 16." https://nozebra.ipapercms.dk/Vestas/Communication/Productbrochure/enventus/enventus/enventus-brochure-2021/?page=16 (accessed Dec. 12, 2021).

[3] "Vestas." https://nozebra.ipapercms.dk/Vestas/Communication/Productbrochure/OffshoreProductBrochure/v236-150-mw-brochure/?page=1 (accessed Dec. 12, 2021).

[4] Z. Faramarzi, S. Abazari, S. Hoghoughi, and N.R. Abjadi, "Improved Power System Dynamic Stability by DFIG in the Presence of SSSC Using Adaptive Nonlinear Multi-Input Backstepping," *J. Oper. Autom. Power Eng.*, Oct. 2022, doi: 10.22098/JOAPE.2023.10565.1753.

[5] M. Nikpayam, M. Ghanbari, A. Esmaeli, and M. Jannati, "Vector Control Methods for Star-Connected Three-Phase Induction Motor Drives Under the Open-Phase Failure," *J. Oper. Autom. Power Eng.*, vol. 10, no. 2, pp. 155-–164, Aug. 2022, doi: 10.22098/JOAPE.2022.8802.1616.

[6] H. Dahmardeh, M. Ghanbari, and S.M. Rakhtala, "A Novel Combined DTC Method and SFOC System for Three-phase Induction Machine Drives with PWM Switching Method," *J. Oper. Autom. Power Eng.*, vol. 11, no. 2, pp. 76-–82, Aug. 2023, doi: 10.22098/JOAPE.2023.9717.1679.

[7] A. Hasanzadeh, H. Shayeghi, and S.R. Mousavi-Aghdam, "A New Fuzzy Direct Power Control of Doubly-Fed Induction Generator in a Wind Power System," *J. Oper. Autom. Power Eng.*, vol. 10, no. 3, pp. 179-–188, Dec. 2022, doi: 10.22098/JOAPE.2022.7662.1545.

[8] S. Karad and R. Thakur, "Recent Trends of Control Strategies for Doubly Fed Induction Generator Based Wind Turbine Systems: A Comparative Review," *Arch. Comput. Methods Eng.*, vol. 28, no. 1, pp. 15-–29, Jan. 2021, doi: 10.1007/s11831-019-09367-3.

[9] A. Dejamkhooy and A. Ahmadpour, "Torque Ripple Reduction of the Position Sensor-less Switched Reluctance Motors Applied in the Electrical Vehicles," *J. Oper. Autom. Power Eng.*, vol. 11, no. 4, 2022, doi: 10.22098/JOAPE.2022.9908.1694.

[10] H. Mohamed, B. Abdelmadjid, and B. Lotfi, "Improvement of Direct Torque Control Performances for Induction Machine Using a Robust Backstepping Controller and a New Stator Resistance Compensator," *Eur. J. Electr. Eng.*, vol. 22, no. 2, pp. 137-–144, Apr. 2020, doi: 10.18280/EJEE.220207.

[11] V. Utkin, A. Poznyak, Y. Orlov, and A. Polyakov, "Conventional and high order sliding mode control," *J. Franklin Inst.*, vol. 357, no. 15, pp. 10244–10261, Oct. 2020, doi: 10.1016/J.JFRANKLIN.2020.06.018.

[12] Z. Liao, Y. Hao, T. Guo, B. Lv, and Q. Wang, "Second-Order Sliding Mode Control of Permanent Magnet Synchronous Motor Based on Singular Perturbation," *Energies*, vol. 15, no. 21, p. 8028, Oct. 2022, doi: 10.3390/EN15218028.

[13] O. Kaplan and F. Bodur, "Second-order sliding mode controller design of buck converter with constant power load," *Int. J. Control*, 2022, doi: 10.1080/00207179.2022.2037718.

[14] I. Matraji, K. Al-Wahedi, and A. Al-Durra, "Higher-Order Super-Twisting Control for Trajectory Tracking Control of Skid-Steered Mobile Robot," *IEEE Access*, vol. 8, pp. 124712-–124721, 2020, doi: 10.1109/ACCESS.2020.3007784.

[15] A. Levant, "Higher-order sliding modes, differentiation and output-feedback control," *Int. J. Control*, vol. 76, no. 9-–10, pp. 924-–941, May 2003, doi: 10.1080/0020717031000099029.

[16] K. Tahir, T. Allaoui, M. Denai, S. Mekhilef, C. Belfedal, and M. Doumi, "Second-order sliding mode control of wind turbines to enhance the fault-ride through capability under unbalanced grid faults," *Int. J. Circuit Theory Appl.*, vol. 49, no. 7, pp. 1959-–1986, Jul. 2021, doi: 10.1002/CTA.3023.

[17] D. Celik, H. Ahmed, and M.E. Meral, "Kalman Filter-Based Super-Twisting Sliding Mode Control of Shunt Active Power Filter for Electric Vehicle Charging Station Applications," *IEEE Trans. Power Deliv.*, 2022, doi: 10.1109/TPWRD.2022.3206267.

[18] G.V. Hollweg, P.J.D. de Oliveira Evald, R.V. Tambara, and H.A. Gründling, "A Robust Adaptive Super-Twisting Sliding Mode Controller applied on grid-tied power converter with an LCL filter," *Control Eng. Pract.*, vol. 122, p. 105104, May 2022, doi: 10.1016/J.CONENGPRAC.2022.105104.

[19] S.M. Rakhtala and A. Casavola, "Real-Time Voltage Control Based on a Cascaded Super Twisting Algorithm Structure for DC-DC Converters," *IEEE Trans. Ind. Electron.*, vol. 69, no. 1, pp. 633-–641, Jan. 2022, doi: 10.1109/TIE.2021.3051551.

[20] M.M. Alhato, S. Bouallègue, and H. Rezk, "Modeling and Performance Improvement of Direct Power Control of Doubly-Fed Induction Generator Based Wind Turbine through Second-Order Sliding Mode Control Approach," *Math. 2020*, vol. 8, no. 11, p. 2012, Nov. 2020, doi: 10.3390/MATH8112012.

[21] B. Kelkoul and A. Boumediene, "Stability analysis and study between classical sliding mode control (SMC) and super twisting algorithm (STA) for doubly fed induction generator (DFIG) under wind turbine," *Energy*, vol. 214, p. 118871, Jan. 2021, doi: 10.1016/J.ENERGY.2020.118871.

[22] Z. Dekali, L. Baghli, and A. Boumediene, "Improved Super Twisting Based High Order Direct Power Sliding Mode Control of a Connected DFIG Variable Speed Wind Turbine," *Period. Polytech. Electr. Eng. Comput. Sci.*, vol. 65, no. 4, pp. 352-–372, Oct. 2021, doi: 10.3311/PPEE.17989.

[23] Y.Q. Pei, H.B. Gu, K.X. Liu, and J.H. Lü, "An overview on the designs of distributed observers in LTI multi-agent systems," *Sci. China Technol. Sci.*, vol. 64, no. 11, pp. 2337-–2346, 2021, doi: 10.1007/s11431-020-1790-3.

[24] A. Gholipour, M. Ghanbari, E. Alibeiki, and M. Jannati,

"Sensorless FOC Strategy for Current Sensor Faults in Three-Phase Induction Motor Drives," *J. Oper. Autom. Power Eng.*, vol. 11, no. 1, pp. 1-–10, Apr. 2023, doi: 10.22098/JOAPE.2022.9274.1648.

[25] S.J. Arand, "Optimization of PM Segments Shift Angles for Minimizing the Cogging Torque of YASA-AFPM Machines Using Response Surface Methodology," *J. Oper. Autom. Power Eng.*, vol. 9, no. 3, pp. 203-–212, 2021, doi: 10.22098/joape.2021.7648.1542.

[26] Z.H. Liu, J. Nie, H.L. Wei, L. Chen, X.H. Li, and M.Y. Lv, "Switched PI Control Based MRAS for Sensorless Control of PMSM Drives Using Fuzzy-Logic-Controller," *IEEE Open J. Power Electron.*, vol. 3, pp. 368-–381, 2022, doi: 10.1109/OJPEL.2022.3182053.

[27] X. Yan and M. Cheng, "An MRAS Observer-Based Speed Sensorless Control Method for Dual-Cage Rotor Brushless Doubly Fed Induction Generator," *IEEE Trans. Power Electron.*, vol. 37, no. 10, pp. 12705-–12714, Oct. 2022, doi: 10.1109/TPEL.2022.3172362.

[28] Y. Cheng and C. Li, "Luenberger Observer-Based Microgrid Control Strategy for Mixed Load Conditions," *Energies 2022*, vol. 15, Page 3655, May 2022, doi: 10.3390/EN15103655.

[29] M.M. Share Pasand and A.A. Ahmadi, "Performance evaluation and simulation of cubic observers," *ISA Trans.*, vol. 122, pp. 172-–181, Mar. 2022, doi: 10.1016/J.ISATRA.2021.04.032.

[30] A.H. Al-Bayati, "Determination of Model, Implement and Compare New Two Optimal Adaptive Fault Diagnosis Observers with Six Observers," *Nov. Res. Asp. Math. Comput. Sci.*, vol. 1, pp. 48-–72, Apr. 2022, doi: 10.9734/BPI/NRAMCS/V1/3115E.

[31] S.S. Tabatabaei, M. Tavakoli, and H.A. Talebi, "A finite-time adaptive order estimation approach for non-integer order nonlinear systems," *ISA Trans.*, vol. 127, pp. 383-–394, Aug. 2022, doi: 10.1016/J.ISATRA.2021.08.034.

[32] S. Mao, C. Ma, X. Zhang, and W. Liu, "Comparison of Nonlinear Observers for the Back Electromotive Force of the Main Exciter of the Brushless Synchronous Starter/Generator," *2022 25th Int. Conf. Electr. Mach. Syst.*, pp. 1-–5, Nov. 2022, doi: 10.1109/ICEMS56177.2022.9983455.

[33] M. Kordestani, M. Mousavi, A. Chaibakhsh, M. Orchard, K. Khorasani, and M. Saif, "A New Compressor Failure Prognostic Method using Nonlinear Observers and a Bayesian Algorithm for Heavy-Duty Gas Turbines," *IEEE Sens. J.*, pp. 1-–1, 2023, doi: 10.1109/JSEN.2022.3233585.

[34] P.H. Rangegowda, J. Valluru, S.C. Patwardhan, and S. Mukhopadhyay, "Simultaneous and sequential state and parameter estimation using receding-horizon nonlinear Kalman filter," *J. Process Control*, vol. 109, pp. 13-–31, Jan. 2022, doi: 10.1016/J.JPROCONT.2021.11.003.

[35] B. Chen, L. Zhang, H. Chen, K. Liang, and X. Chen, "A novel extended Kalman filter with support vector machine based method for the automatic diagnosis and segmentation of brain tumors," *Comput. Methods Programs Biomed.*, vol. 200, p. 105797, Mar. 2021, doi: 10.1016/J.CMPB.2020.105797.

[36] M.V. Satya Sai Chandra and S. Mohapatro, "Active sensor fault tolerant control of bus voltage in standalone low voltage DC microgrid," *Electr. Eng.*, pp. 1—14, Dec. 2022, doi: 10.1007/S00202-022-01716-Z/FIGURES/21.

[37] H. Wang, Q. Wang, H. Zhang, and J. Han, "H-Infinity Observer for Vehicle Steering System with Uncertain Parameters and Actuator Fault," *Actuators 2022*, vol. 11, no. 2, p. 43, Jan. 2022, doi: 10.3390/ACT11020043.

[38] E. Shahzad, A.U. Khan, M. Iqbal, A. Saeed, G. Hafeez, et al., "Sensor Fault-Tolerant Control of Microgrid Using Robust Sliding-Mode Observer," *Sensors 2022*, vol. 22, no. 7, p. 2524, Mar. 2022, doi: 10.3390/S22072524.

[39] Q. Lin, L. Liu, and D. Liang, "Hybrid Active Flux Observer to Suppress Position Estimation Error for Sensorless IPMSM Drives," *IEEE Trans. Power Electron.*, vol. 38, no. 1, pp. 872-–886, Jan. 2023, doi: 10.1109/TPEL.2022.3203815.

[40] O. Naifar and G. Boukettaya, "On Observer Design of Systems Based on Renewable Energy," *Stud. Syst. Decis. Control*, vol. 410, pp. 135-–176, 2022, doi: 10.1007/978-3-030-92731-8_8/FIGURES/30.

[41] X. Meng, H. Yu, J. Zhang, T. Xu, H. Wu, and K. Yan, "Disturbance Observer-Based Feedback Linearization Control for a Quadruple-Tank Liquid Level System," I*SA Trans.*, vol. 122, pp. 146-–162, Mar. 2022, doi: 10.1016/J.ISATRA.2021.04.021.

[42] H. Xu, S. Liu, B. Wang, and J. Wang, "Distributed Observer for Affine Nonlinear Systems and its Application on Automated Highway System," *IEEE Trans. Intell. Veh.*, 2022, doi: 10.1109/TIV.2022.3163773.

[43] M. Zolfaghari, G.B. Gharehpetian, M. Shafie-khah, and J.P.S. Catalão, "Comprehensive review on the strategies for controlling the interconnection of AC and DC microgrids," *Int. J. Electr. Power Energy Syst.*, vol. 136, p. 107742, Mar. 2022, doi: 10.1016/J.IJEPES.2021.107742.

[44] Y. Xiao, X. Pan, and T.T.Y. Yang, "Nonlinear backstepping hierarchical control of shake table using high-gain observer," *Earthq. Eng. Struct. Dyn.*, vol. 51, no. 14, pp. 3347-–3366, Nov. 2022, doi: 10.1002/EQE.3726.

[45] M.S. Haider Khan and S. Kumar Mallik, "Mechanical sensorless control of a rotor-tied DFIG wind energy conversion system using a high gain observer," *J. King Saud Univ. Eng. Sci.*, 2022, doi: 10.1016/J.JKSUES.2022.05.005.

[46] C. Lascu and G.D. Andreescu, "PLL position and speed observer with integrated current observer for sensorless PMSM drives," *IEEE Trans. Ind. Electron.*, vol. 67, no. 7, pp. 5990-–5999, Jul. 2020, doi: 10.1109/TIE.2020.2972434.

[47] M.R. Kafi, M.A. Hamida, H. Chaoui, and R. Belkacemi, "Sliding Mode Self-Sensing Control of Synchronous Machine Using Super Twisting Interconnected Observers," *Energies 2020*, vol. 13, no. 16, p. 4199, Aug. 2020, doi: 10.3390/EN13164199.

[48] M. Zhang, Z.T. Li, Q.M. Wu, B. Dahhou, and M. Cabassud, "Actuator fault diagnose for interconnected system via invertibility," *Int. J. Model. Identif. Control*, vol. 33, no. 4, pp. 283—298, 2019, doi: 10.1504/IJMIC.2019.107487.

[49] M.A. Hamida, J. De Leon-Morales, and A. Messali, "Observer design for nonlinear interconnected systems: experimental tests for self-sensing control of synchronous machine," *Int. J. Adv. Manuf. Technol.*, vol. 105, no. 1-–4, pp. 1041-–1054, Nov. 2019, doi: 10.1007/S00170-019-04253-5/FIGURES/12.

[50] K. Wu, "Sensorless Control of PMSM via Extended State Interconnected Observer," A*SCC 2022 - 2022 13th Asian Control Conf. Proc.*, pp. 979—984, 2022.

[51] A.P. Schaffarczyk, Introduction to wind turbine aerodynamics, 2020th ed. Springer, 2020.

[52] Y. Sun, S. Yan, B. Cai, Y. Wu, and Z. Zhang, "MPPT Adaptive Controller of DC-based DFIG in Resistances Uncertainty," *Int. J. Control. Autom. Syst.*, vol. 19, no. 8, pp. 2734-–2746, Aug. 2021, doi: 10.1007/S12555-020-0302-3/METRICS.

[53] B.P. Ganthia and S.K. Barik, "Steady-State and Dynamic Comparative Analysis of PI and Fuzzy Logic Controller in Stator Voltage Oriented Controlled DFIG Fed Wind Energy Conversion System," *J. Inst. Eng. Ser. B*, vol. 101, no. 3, pp. 273-–286, Jun. 2020, doi: 10.1007/S40031-020-00455-8/TABLES/4.

[54] R. Sadeghi, S.M. Madani, S. Member, M. Ataei, M.R.A. Kashkooli, and S. Ademi, "Super - Twisting Sliding Mode Direct Power Control of Brushless Doubly Fed Induction Generator," *IEEE Trans. Ind. Electron.*, vol. 0046, no. VC, 2018, doi: 10.1109/TIE.2018.2818672.

[55] G. Abad, J. Lopez, M. Rodriguez, L. Marroyo, and G. Iwanski, Doubly fed induction machine: modeling and control for wind energy generation. John Wiley & Sons,

2011.